Discover Nano

REVIEW Open Access

Recent advances of MXene/chitosan nanocomposites for industrial applications

Shaikh Almoon Hussain[1†], Md. Hanif Munshi[1,2†], Md. Kamruzzaman[1*], Md Nasiruddin[3], Mohammad Rafiqur Rashid[4] and Tarikul Islam[5,6*]

†Shaikh Almoon Hussain, Md. Hanif Munshi contributed equally to this work and they are joint first authors.

*Correspondence:
Md. Kamruzzaman
mkamruzzamandu81@gmail.com
Tarikul Islam
tarikul.mbstu@gmail.com

Full list of author information is available at the end of the article

Abstract

MXene/chitosan (MX/CS) composites have recently garnered significant attention due to their unique properties. This synergistic integration has opened new opportunities for various industrial applications. This review provides a comprehensive analysis of recent advancements in the use of MX/CS composites across multiple sectors, including electromagnetic interference (EMI) shielding, electrochemical sensing, water treatment, fire-retardant materials, environmental remediation, and energy storage devices such as supercapacitors and batteries. Each application has its own requirements and standards for the chosen building materials. Fortunately, all the divergent requirements can be achieved in MXene (MX) and chitosan (CS) by relatively moderate treatment. The discussion highlights how the unique interactions between MX nanosheets and CS matrices enhance performance characteristics. Despite these advantages, several critical challenges remain, including long-term stability, material scalability, and cost-effective manufacturing processes. This review summarizes recent advancements by identifying key research gaps and aims to guide further innovation in the fields. The potential of MX/CS composites to contribute to sustainable and high-performance industrial solutions is undeniable, provided that existing challenges are met with innovative approaches.

Keywords Nanocomposites, Industrial applications, Wastewater treatment, Sensors, EMI shielding, Solar evaporation

1 Introduction

MXene (MX) has long held a dominant position in research and technology [1]. MX and its derivatives demonstrated extensive effectiveness in sensors [2], wastewater treatment [3], supercapacitors [4], batteries [5], electromagnetic interference shielding (EMI) [6], solar evaporation [7], solvent dehydration [8], and fire hazard prevention [9]. MX fits suitably in those applications because of their larger contact area, enhanced structural durability, hydrophilic nature, and flexibility of surface alteration. These materials are biocompatible, have many surface-tailored functional groups, can absorb EMI radiation, transform light into heat, have higher metallic conductivity, high mechanical strength, high thermal stability, and a notable negative zeta potential, among many other

noteworthy properties [10–13]. MX-biopolymer nanocomposites, including MX/cellulose [14], MX/chitosan [15], MX/alginate [16], MX/lignin [17], MX/starch [18], and MX/natural rubber [19], have been created to improve the aforementioned MX qualities. Concerning its inexpensiveness, renewable nature, ease of availability, hydrophilicity, biocompatibility, biodegradability, and abundance of programmable functional groups, chitosan has been widely adopted as a foundation for novel MX/CS composites [20–23]. This review aimed to discuss the recent advancements of MX/CS composite applications.

Researchers in the materials sciences are particularly fascinated by MX, a family of two-dimensional (2D) in nature transition metal carbides, nitrides, and carbonitrides that were originally identified by Drexel University researchers in 2011. This new material class began with the first synthesis of $Ti_3C_2T_x$, which was produced by selectively etching aluminum layers from MAX phases, which is usually denoted as $M_{n+1}AX_n$. The general formula $M_{n+1}X_nT_x$, commonly used to describe MXs, where "M" layer is a transition metal, "X" layer is either carbon or nitrogen. At the same time, "T_x " indicates exterior expulsion (such as –OH, –O, or –F), and "A" layer refers to the elements from group 13 or 14 [24–27]. In contrast to the less durable metal–metal connection, the strong metal–carbon link may be preserved with the use of strong etching acids. This result produces a 2D layered material, which is still the most significant finding of the past ten years. As the MAX family continues to develop, the categorization of M, A, X, T_x, and n elements is changing. The number of MAX precursors in this family has significantly increased and is still growing [28–30]. MXs features an extensive expanse of surface, hydrophilicity, and metallic conductivity, which distinguishes them from other 2D materials. Their composition, structure, and surface terminations may all be changed to customize their tunable electrical, optical, and electrochemical characteristics. In addition, MXs has tremendous durability due to Young's modulus values topping 300 GPa, which meets the criteria for use in flexible electronic devices and reinforced composites [31–34].

The compositional variety of MXs accounts for its adaptability; more than 30 variations have been synthesized, and hundreds more are predicted theoretically. For specific applications, such as supercapacitors or sensors, this tunability enables customization of the electrical, optical, and catalytic characteristics [35, 36]. Problems still exist, though, such as oxidative instability in aqueous conditions that restricts long-term performance and industrial scalability concerns since existing techniques depend on dangerous hydrofluoric acid (HF) or its precursors [37, 38]. Despite their exceptional qualities, MXs have several drawbacks. Their synthesis raises safety and environmental issues because it calls for using dangerous etchants like HF. Additionally, MXs are susceptible to oxidation, which may impair their functionality over time. To increase their stability and durability, methods including surface modification and controlled synthesis are being studied and explored [24, 39, 40].

Chitosan (CS), a cationic polysaccharide produced from chitin (CT) by deacetylation, is intensively explored in materials science for its extraordinary features, including biocompatibility, biodegradability, and antibacterial activity [41, 42]. It is structurally composed of N-acetyl-D-glucosamine and β-(1→4)-linked D-glucosamine units, providing many amino and hydroxyl groups. Flexibility of CS is supported by these functional groups, which allow for chemical modification, metal ion chelation, and interaction with

a variety of substrates, making it a valuable material in many different fields [43, 44]. It is an excellent matrix for nanocomposites because of its cationic character, caused by protonated amino groups, allowing electrostatic interactions with anionic species. CS expands its uses in industrial applications, energy storage, and environmental cleanup by improving mechanical strength, electrical conductivity, and usefulness when mixed with conductive nanomaterials [45, 46]. The polycationic nature of CS facilitates electrostatic interactions with negatively charged surfaces in acidic to neutral environments. This electrostatic attraction offers a reliable and non-covalent technique for stabilizing and dispersing nanoparticles inside a CS matrix [47, 48]. CS maximizes the functional qualities of the nanoparticles by avoiding agglomeration, which guarantees a larger surface area. Additionally, the film forming ability of CS makes it possible to create composite materials with evenly implanted nanoparticles, which produce synergistic benefits [49, 50]. Because of its special qualities, like biocompatibility, customizable surface chemistry, and incredible tendency and ability to form films, CS is a perfect companion for MX and other nanoparticles, allowing for the creation of multifunctional nanocomposites with specialized characteristics for cutting-edge uses [51, 52].

Because of its special qualities and benefits, the MX/CS composite performs exceptionally well in industrial applications. The strong mechanical durability, thermal stability, and electrical conductivity of MX combine well with the antibacterial, biodegradable, and biocompatible qualities of CS [53–55]. It is perfect for energy storage, biomedical equipment, and water purification because of this synergy, which improves durability, usefulness, and environmental friendliness. Utilizing electrostatic interactions, the synthesis techniques of the composite are successful and well accepted, guaranteeing scalability and cost-effectiveness for a range of industrial requirements [56–58].

The stability and dispersion of the composite are improved by electrostatic interactions between the positive charge of CS and the negative surface of MX. The functional groups improve the compatibility and integration of the two materials in composite scaffolds by facilitating hydrogen bonding and electrostatic interactions with the hydroxyl and amino groups of CS. CS can be intercalated into MX layers to improve their mechanical and functional qualities by preventing restacking. To make MX/CS interactions stronger, functionalization techniques such covalent bonding and silane coupling are employed [59–62]. In watery conditions, CS reduces MX oxidation by acting as a protective matrix. Because of their strong interfacial bonding, composites retain their structural integrity under mechanical stress. By improving the dispersion of MX nanosheets within the CS matrix, interlayer changes in MX may be tailored to promote uniform composite production and increase mechanical properties [63–65]. While CS enhances overall biodegradability, pure MXs are not biodegradable by nature. Biodegradability and structural integrity are intended to be balanced in the MX/CS composite. While the durability of MX offers enough support during the bone healing process, the biodegradable nature of CS guarantees the progressive breakdown of the scaffold [66–68]. Films of MX/CS maintain their excellent conductivity. Because CS is hydrophilic, conductivity is humidity-sensitive and decreases with increasing humidity. Compared to CS alone, which is susceptible to thermal breakdown at high temperatures, the addition of MX to CS scaffolds probably improves the composthermal resilience of the composite. At low concentrations, Ti-based MXs (such as $Ti_3C_2T_x$) are non-toxic and biocompatible. Because CS lessens the possible cytotoxicity of MX, composites can be

used for implants and wound healing. MX/CS composites exhibit > 80% cell viability in in-vitro experiments [69–71]. Consequently it is very clear that the study of the MX/CS composites is relatively low in contrast of its assumed potential. In this review work we discussed the implication, success and development possibilities of MX/CS composite in several industrial applications which are non-biomedical and non-biological fields.

2 Chitosan synthesis

2.1 Isolation of chitin (CT)

The polymer chain of N-acetylglucosamine (a glucose derivative) is called chitin $(C_8H_{13}O_5N)_n$. Crustacean shells (shrimp, crabs, lobsters, crayfish, krill, and barnacles) are the primary source of CT. Fungi and insects are occasionally seen as sources and mostly composed of proteins, CT, and calcium carbonate, such as crustacean shells. CT must be separated from the other components of the shell to be extracted. In general, extraction procedures fall into two categories: chemical or biological. Deproteinization is another term for the CT separation process [72–75].

2.1.1 Chemical methods

Acetone, ethyl alcohol, and diethyl ether are the organic solvents used in decolorization, which endures for 0.5–12 hours at 20–60 °C. Demineralization, the subsequent step, frequently involves dissolving $CaCO_3$ in the shell by reacting with a strong acid, like hydrochloric acid (HCl) solution at up to 10% w/v, for 2-24 hours while stirring. Deproteinization is the next stage, which entails dissolving proteins in a 1–10% (w/w) aqueous alkali solution (such as NaOH, KOH, Na_2SO_3, and Na_2CO_3) at 65–100 °C for 0.5–24 hours [76–78].

2.1.2 Biological method

Demineralization is achieved by fermenting with lactic acid or microorganisms that produce lactic acid, then incubating for a few hours at 20–37 °C and pH 6–7. Then, chitooligosaccharides are created by deproteinization using enzymes (cellulases, pectinases, chitinases, lipases, papain, hemicellulases, pepsin, and lysozyme). Protein deproteinization in HCl solution at pH 6–8.5 and 30–55 °C for up to 24 hours. Centrifugation or filtering is used to extract the produced chitin from the reaction mixture, and then washing procedures are carried out to eliminate any leftover enzyme, substrate, or buffer components [79–82].

2.2 Synthesis of CS from CT

Deacetylation transforms CT into CS. The acetyl groups attached to the amino group must be eliminated to expose the $-NH_2$ groups [83]. The degree of acetylation (DA), which also significantly affects its mechanical, physicochemical, and biological properties, is a crucial determinant of whether it is categorized as CT or CS. The polymer generated by the deacetylation process contains both glucosamine units and N-acetyl-glucosamines units [84, 85]. A polymer generated via deacetylation and containing more than 50% N-acetyl-glucosamine units is still referred to as CT; if not, it is termed CS [86]. A simplified schematic representation of CS synthesis is shown in Fig. 1.

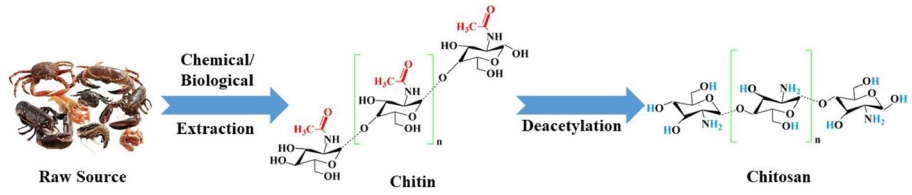

Fig. 1 Synthesis of chitosan from chitin (created with Canva)

2.2.1 Chemical methods

Highly concentrated NaOH solutions, usually 40–60% (w/v), however, depending on the desired deacetylation degree (DD), concentrations as low as 20% or as high as 80% may be utilized. Sometimes other bases are used, such as lithium hydroxide (LiOH) or potassium hydroxide (KOH). 80–140 °C; the industry norm for effective deacetylation is 100—120 °C. More extended periods or catalysts are needed at lower temperatures (50–80 °C). 1-24 hours, depending on the temperature and concentration of NaOH. To modify pH and remove the byproducts of CH_3COONa and NaOH, use water or diluted acids (such as 0.1–1 M HCl or acetic acid). Then, either air-dry at room temperature for 4–24 hours or dry in an oven at 40–80 °C [86–89].

2.2.2 Biological/Enzymatic methods

Microorganisms such as *Vibrio cholerae* and *Colletotrichum lindemuthianum* generate CT deacetylases, which are then refined for utilization. The development of microorganisms requirements determine the temperature and pH, which are normally neutral to slightly alkaline. To eliminate acetyl groups, CT is combined with CT deacetylases in a buffer under carefully monitored circumstances [90–92]. The pH range for an enzymatic process is typically 7–12 hours and lasts 24–48 hours. The temperature range is 37–60 °C. Buffers such as 50 mM Tris–HCl are frequently used with the enzyme and CT substrate. Surfactants or solubilizing agents are occasionally used to enhance reaction efficiency, particularly when working with insoluble CT [93, 94].

3 MXene synthesis

3.1 Top–down approach

At this point, over 20 MXs ($M_{n+1}X_nT_x$) have been synthesized, and over 70 distinct MAX phases ($M_{n+1}AX_n$) have been produced experimentally. The substantial demand for MX in materials development research sparked much interest among scientists in the MAX phase etching process. Through the separation of "M" and "A," "top-down" selective etching techniques convert the MAX phase into MX. MAX phases are held together firmly by a stronger van der waals interaction and a more resilient metallic M-A connection [95, 96]. This etching reaction is susceptible to air and moisture (< 1 ppm H_2O; < 5 ppm O_2). Etching agents can be categorized as fluoride salt (LiF, KF, NH_4F), molten salts (LiF + KF, $CdBr_2$, $ZnCl_2$), alkalis (NaOH), acids (HF, H_3PO_4), and others. Fluoride salt (LiF, KF, NH_4F) + HCl affects the synthesis of multi-layered MXs when the intercalation manufacturing process is used. In other words, the combination of etching agents widens the interlayer space by weakening interflake connections and raising the lattice parameter [97, 98]. Some of the most common structures of the MAX phase are shown in Fig. 2a, along with a simple illustration of the most common routes to synthesize MX from the MAX phase in Fig. 2b.

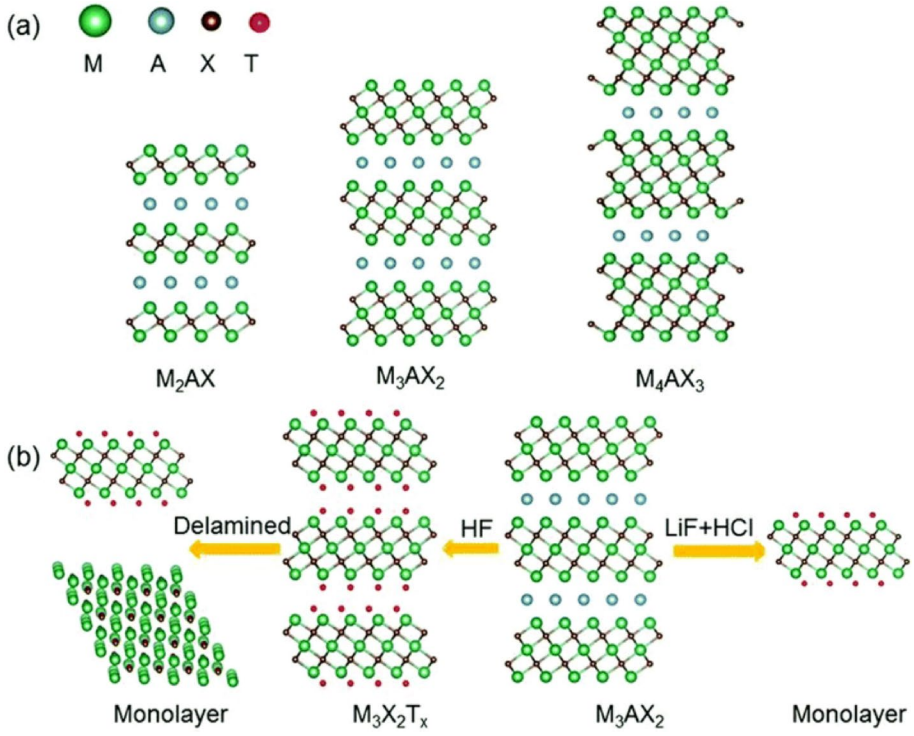

Fig. 2 (a) M_2AX, M_3AX_2, and M_4AX_3 phase crystal structures. (b) LiF + HCl etching for monolayer MXs or HF etching for multilayer MXs. Reproduced with permission [100] Copyright 2019, Royal Society of Chemistry

3.1.1 Etching by HF solution

In an early study by Naguib et al. [99], they synthesized $Ti_3C_2T_x$ MX from Ti_3AlC_2 at room temperature for 2 hours using a 50% HF etching solution, yielding an incredible yield percentage of almost 100%.

A different batch of MXs was treated with 50% concentrated HF at ambient temperature for 96 hours while being agitated at 200 rpm. The etched MXs were referred to as multilayer MXs after being repeatedly cleaned using centrifugation at 4500 rpm until the pH level reached 4. Here, 1-methyl-2-pyrrolidinone treatment was used to create a few layers of V_2CT_x, and tetrabutylammonium hydroxide (TBAOH) intercalation treatment was used to create the inter-sheet gap. Figure 3a illustrates the HF etching phase transition explanation [101].

In another study, Nb_2CT_x was synthesized by etching Nb_2AlC at room temperature for 90 hours using a 50% concentrated HF etching solution. The research team was able to achieve 100% yield in that study [102].

3.1.2 HCl/Fluoride salt mixture etching

Halim et al. described a study that used selective etching of gallium from Mo_2Ga_2C precursor to produce massive amounts of molybdenum carbide (Mo_2CT_x) MX. Etching was carried out by a solution of 3 M LiF and 12M HCl. TBAOH was then used to continue the intercalation process, and finally, delamination was finished. Heat treatment between 300 and 1000 K caused the produced Mo_2CT_x to behave like a semiconductor; on the other hand, it behaved like a metal. Figure 3b shows the synthesis processes (etching, delamination, and filtering) [103].

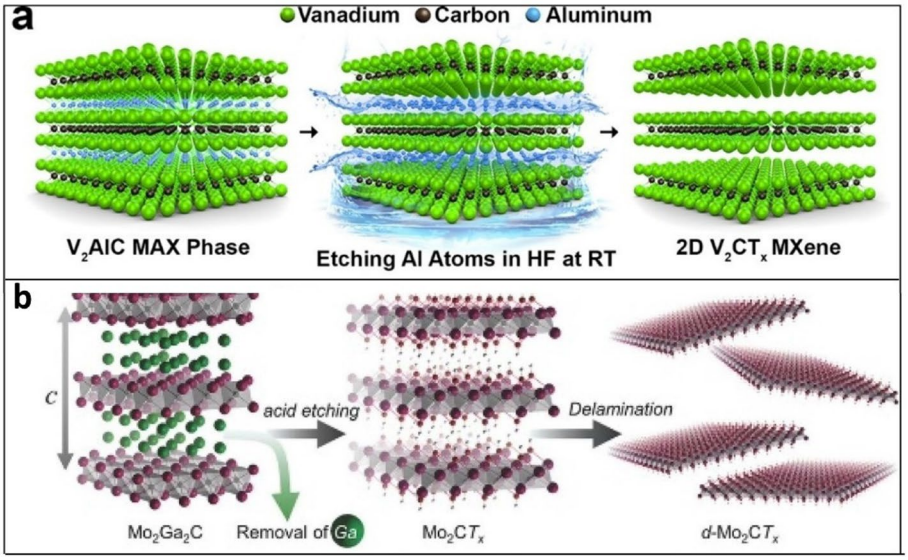

Fig. 3 (a) Diagrammatic illustration of the synthesis of V_2CT_x from V_2AlC. Reproduced with permission [101] Copyright 2017, American Chemical Society; (b) Mo_2Ga_2C MAX phase etching and delamination schematic. Reproduced with permission [103] Copyright 2016, Wiley-VCH Verlag

In another approach to synthesize $Ti_3C_2T_x$ MX from Ti_3AlC_2, [104] Sang et al. conducted another investigation in which he dissolved 1g of LiF in 20mL of 6 M HCl in a 100 mL polypropylene plastic vial. The team then gradually added 1 g of Ti_3AlC_2 and let the reaction run for 24 hours at 35 °C. After centrifuging at 3500 rpm for 1 hour at the same speed, a dark green supernatant solution of big $Ti_3C_2T_x$ flakes was obtained, indicating that the acidic product had been thoroughly cleaned with DI H_2O until the pH reached 6. $Ti_3C_2T_x$ colloidal solution up to 1.5 mg/mL was collected.

3.1.3 Molten salt-based etching

The water dispersible $Ti_3C_2T_z$ MX, which was produced without the use of HF, lacked the -OH terminal group. Here, stannous fluoride (SnF_2) molten salt was used as a selective etchant to create $Ti_3C_2T_z$ MX from the Ti_3AlC_2 MAX precursor. SnF_2 and Ti_3AlC_2 were heated to 550 °C for 6 hours to conduct the molten salt etching procedure. Resulting in the development of certain Sn spheres and $Ti_3C_2T_z$ clay. After etching, the $Ti_3C_2T_z$ clay was washed with a KOH solution to dissolve any excess or unreacted SnF_2 crystals. KOH-washed $Ti_3C_2T_z$ clay was intercalated with dimethyl sulfoxide (DMSO) and rinsed off with water. After intercalation, the $Ti_3C_2T_z$ clay was delaminated by bath sonication, and a stable dispersion of $Ti_3C_2T_z$ nanosheets was obtained by centrifuging the delaminated $Ti_3C_2T_z$ dispersion [105].

In another study by L. Liu et al. [106], Ti_3AlC_2 was utilized as the MAX phase precursor, while $CuCl_2$, NaCl, and KCl were selected as the molten salts. To guarantee homogeneity, a conventional procedure was to combine Ti_3AlC_2 with molten salt in the following ratio: Ti_3AlC_2:$CuCl_2$:NaCl:KCl = 1:3:2:2 in molar ratio. The mixture was then ground thoroughly for ten minutes in the air. After that, the mixture was cooked for 24 hours at 680 °C in a tube furnace with argon flowing through it. The reddish-brown materials were washed with deionized water and then collected using vacuum filtering. Finally, $Ti_3C_2T_x$ MX was created after being dried in a vacuum oven for a whole night at 80 °C.

3.2 Bottom-up approach

The most widely used technique for producing relatively pure materials with a controlled structure at the atom or nanoscale level for the past 30 years is chemical vapor deposition (CVD), which is achieved by the chemical reactions of gaseous reactants in an active (heat, light, plasma) environment [107, 108]. Xu et al. initially suggested a bottom-up synthesis approach in 2015, employing CVD to directly create large-size (more than 100 microns) and ultra-thin (several nanometers thick) α-Mo_2C crystals. Methane is the source of carbon, while the molybdenum foil beneath the copper foil is the source of molybdenum (the two foils together make up a bimetal foil). When the temperature rises over 1085 °C, Cu melts, and Mo atoms diffuse to the surface, where they combine with the carbon atoms produced by methane breakdown to directly create Mo_2C crystal. The lateral dimensions of Mo_2C produced by the CVD process were at the centimeter level two years later [109]. The CVD synthesis process of MX synthesis is shown in Fig. 4.

4 Application of MX/CS composite

4.1 Electromagnetic interface (EMI) shielding

Disturbances carried on by electromagnetic radiation are known as EMI, and they can interfere with the functionality of electronic equipment. EMI can be conducted or emitted. EMI shielding is essential because it shields delicate electronics from outside interference and guarantees their dependable operation, especially in vital systems like communication and medical equipment [111, 112]. EMI shielding was one of the earliest effective practical applications of MX after its discovery [113]. Additionally, CS is already an established and proven material to shield against EMI. So, it is unsurprising that applying MX/CS composite for EMI shielding draws massive interest among researchers [114]. Regarding research, MX/CS composites shield from EMI by reflecting, absorbing, and scattering many times.

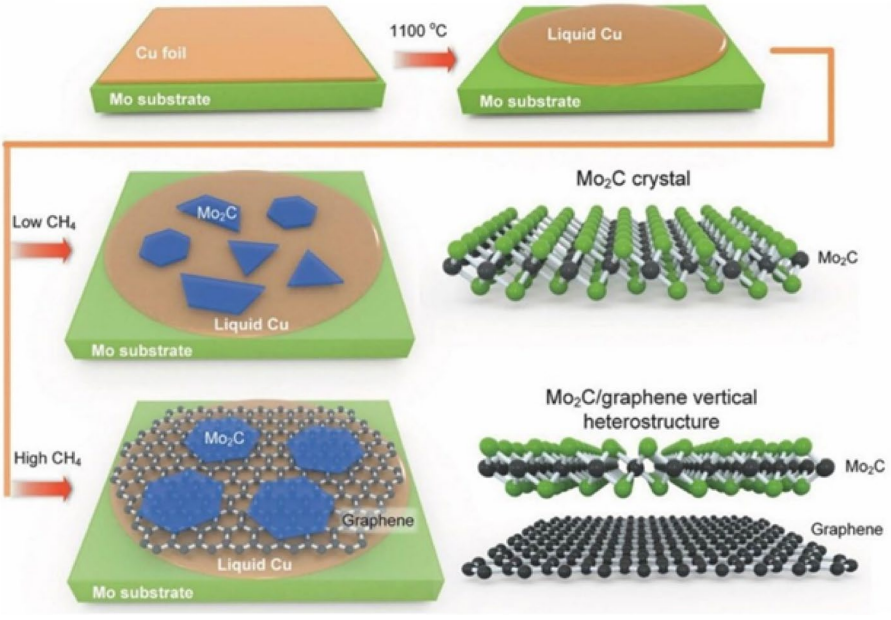

Fig. 4 Diagrammatic representation of the Mo_2C crystal formation process using the CVD method. Reproduced with permission [110] Copyright 2017, Wiley-VCH

MX, especially $Ti_3C_2T_x$, exhibit excellent metallic conductivity. Because of their high conductivity, they may successfully reflect incoming electromagnetic waves (EMW) because they interact with the free electrons in the MX layers. Although the primary function of MXs is reflection, they can aid in EMI shielding by absorption. This happens because the EMW cause currents to flow through the MX layers, which results in conductive losses. Additionally, MXs exterior layer modifications (-O, -OH, and -F) may contribute to polarization losses and improve absorption [115–117]. A combination of the layered MX structures and the inherent porosity of CS allows EMW to be reflected and scattered within, extending their journey and improving energy dissipation. The CS matrix and the layered MX structure combine to provide a complex microstructure with many interactions. This improves shielding efficiency by significantly increasing the likelihood of numerous EMW reflections and dispersion [118, 119].

The structure and conductivity of the composite enable reflection, absorption, and numerous internal reflections, which are the main EMI shielding processes for MX/CS films. A layered morphology is produced by the homogenous dispersion of MX nanosheets in the CS matrix. By encouraging many internal reflections of EMW within the composite, this configuration lengthens the propagation path of the waves and strengthens absorption-dominated attenuation [120–122]. MX acts as a reflecting coating for electromagnetic radiation because of its exceptional electrical conductivity and metallic properties-significant reflection results from the intense interaction between incident EMW and the delocalized electrons in the MX structure. The layered structure of MX and the presence of functional groups (-OH, -O, -F) increase energy absorption by introducing dielectric and conduction losses. Furthermore, absorption processes are facilitated by the interfacial polarization between MX and CS. The 2D layered structure of MX promotes numerous scattering and reflection inside the structure, which raises the overall EMI attenuation efficiency, especially when combined with a porous or hierarchical matrix like CS [61, 123, 124]. When exposed to oxygen or moisture, MX (such as $Ti_3C_2T_x$) are prone to oxidation, breaking down into TiO_2 and amorphous carbon. This is a worrying fact. Over time, this lowers electrical conductivity and jeopardizes EMI shielding effectiveness (SE). Ohmic loss and reflection capacities are reduced when MXs undergo oxidation because they lose their metallic conductivity. The conductive network is disrupted by structural deterioration, which lowers absorption and many internal reflections [125, 126].

Tan et al. conducted a study in which the research team employed a layer-by-layer assembly technique for constructing a sequence of alternate layered films made of CS and MX. The resulting 35 μm thick MX/CS multilayer film exhibits a high specific EMI shielding efficiency (SSEt) of 10.650 dB cm^2/g, and a maximum EMI shielding effectiveness (SE) of 40.8 dB with excellent thermal conductivity (6.3 W/mK) [127]. The MX/CS film casting technique in Fig. 5a and the EMI shielding mechanism of the film shown in Fig. 5b are presented through simple illustrations.

In a separate study focusing on the MX/CS composite as the aerogel, conducted by S. Wu et al., CS hydrogels and MXs were assembled using freeze-drying and an appropriate heating technique to create hierarchically porous hybrid carbon aerogels. The hybrid carbon aerogel also offers fire resistance and considerable thermal insulation (about 25.88 mW/mK at 25 °C and 62.65 mW/mK at 800 °C under Ar) [128]. For a better

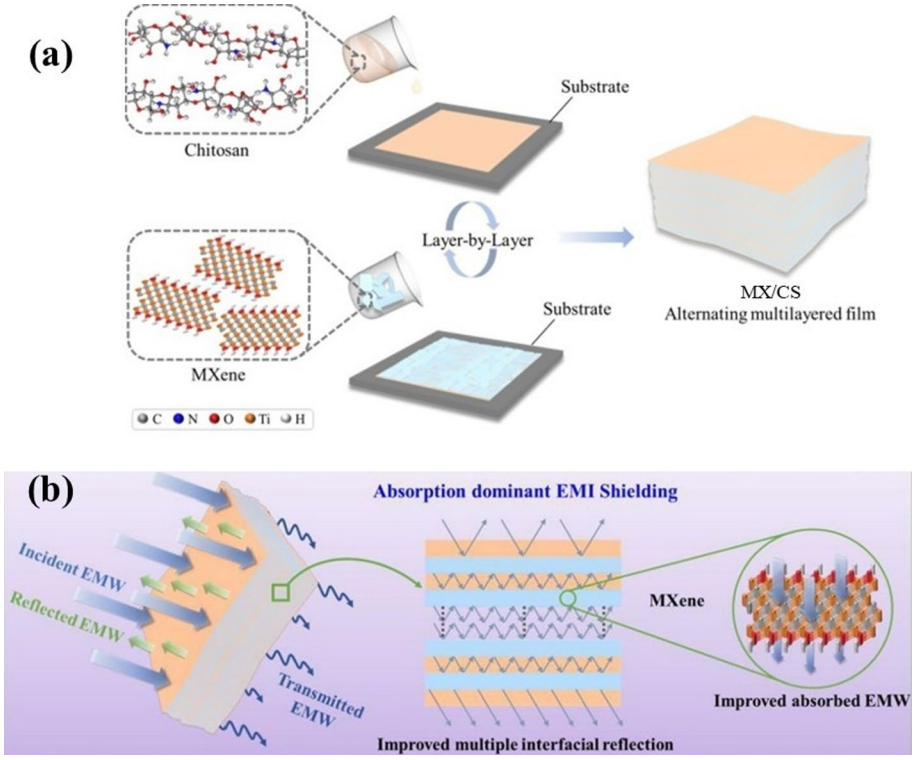

Fig. 5 Illustration of (a) synthesis of multilayered MX/CS film, (b) EMI shielding by multilayered MX/CS film. Reproduced with permission [127] Copyright 2022, Elsevier

understanding of the efficiency of MX/CS composites in EMI shielding, a summary of some recent studies is included in Table 1.

4.2 Electrochemical sensors

MX-based electrochemical sensors record electrical signals from chemical processes involving the target material, such as voltage or current. With regard to the remarkable electrochemical characteristics of MX, excellent electrical conductivity, large surface area, and adaptable chemical structure, these sensors are exceptionally valuable in applications like industry, healthcare, and environmental monitoring [135–137]. MX sensors are also improving in their ability to measure temperature, pressure, strain, and humidity, which is anticipated to be effective for industrial safety [138–140]. MX/CS composite sensors provide a hybrid sensing platform by combining MX and CS. By increasing the stability, dispersibility, and biocompatibility of the composite, CS is appropriate for industrial and biological applications. The sensor functions like other MX-based sensors, measuring electrical signals from target interactions [15, 141]. Usually, the MX/CS composite operates as the electrode or an additional layer on the electrode surface. One other feature of MX/CS composite-based sensors recently developed is self-healing sensing technology [142–144].

4.2.1 Pressure sensor

In a research, Gu et al. created a hierarchical architecture-based MX/CS fiber pressure sensor, which was subsequently used in textiles. They exhibit a wearable, textile pressure sensor composed of MX/CS that is small (about 0.76 mm), light (approximately 0.188 g/

Table 1 A few highlighted examples of MX/CS composites and their use in EMI shielding

Matrix/Composite	Synthesis Method	Efficiency of EMI shielding	References
MX/CS	Film prepared by layer-by-layer assembly technique	Thickness: 35 µm EMI SE: 40.8 dB Specific SE: 10, 650 dB cm^2/g	[127]
MX/CS	Film prepared by Vacuum assisted filtration	Thickness: 37 µm EMI SE: ~ 34.7 ± 0.2 dB Specific SE: 15,153.9 ± 153 dB cm^{-1}	[129]
MX/CS/TiO_2	Aerogel prepared by freeze-drying	Thickness: 3 mm EMI SE: 61.4 dB Specific SE: 5155.46 dB cm^2/g	[128]
MX/CS	Aerogel prepared 3D printing of MX/CS solution	EMI SE: 27 dB	[119]
MX/CS/PVA	Hydrogel prepared by Freeze Drying	Thickness: 1.05 mm EMI SE: 66.7 dB	[118]
MX/CS/MWCNT/XSBR	Aerogel-Film Prepared by Ultrasonic stirring and Vacuum Drying	Thickness: 250 µm EMI SE: 86.32 dB Absorption coefficient = 0.76	[61]
MX/PE-CS	Hydrogels fabricated by ultrasound-assisted dispersion	Thickness: 2 mm EMI SE: 38.40 dB (X-band) 39.70 dB (Ku-band) 45.00 dB (Ka-band) 55.30 dB (THz-band)	[130]
MX/CS/CNT	Porous $Ti_3C_2T_x$/CS/CNT composites were prepared by 3D printing	Thickness: 3 mm EMI SE: 26 dB Specific SE: ~ dB cm^2/g R-A coefficient: 0.72	[131]
MX/TA-CS	MX/TA-CS cotton fabric was fabricated using a layer-by-layer spraying technique	Thickness: 100–200 µm EMI SE: 18–22 dB (X-band)	[120]
MX/CS-AgNW coated TPU	CS-AgNW solution and MXene slurry coated on TPU fabric	Thickness = 2 mm EMI SE_T = 91.9 dB (X-band) EMI SE_A = 86.4 dB (X-band) EMI SE_T = 5.5 dB (X-band)	[132]
MX/PAA-CS	A double network hydrogel was fabricated adapting gel immersion technique	Thickness: 2 mm EMI SE: 73.8 dB (THz band)	[133]
MX/CS/CoFe/MOF	A heterojunction aerogel was fabricated by freeze-drying method	Thickness: 1.5 mm EMI SE: 50.95 dB (C band)	[134]

SE: Shielding Effectiveness, SE_A: Shielding Effectiveness due to Absorption, SE_R: Shielding Effectiveness due to Reflection, SE_T: Total Shielding Effectiveness, PVA: Polyvinyl alcohol, MWCNT: multiwalled carbon nanotubes, XSBR: Carboxylated styrene-butadiene rubber, PE: Polyelectrolyte, CNT: Carbon Nanotube, TA: Thioctic Acid, AgNW: Silver nanowire, TPU: Thermoplastic polyurethane, PAA: Polyacrylic acid, MOF: Metal organic framework

cm^3), and has an ultrawide linear range and great sensitivity. A remarkable sensitivity (1.16 kPa^{-1}) (see Fig. 6b), ultra-wide linear range of 1.5 MPa (Linearity, $R^2 = 0.997$) (see Fig. 6c), minimal depletion over 1000 loading/unloading cycles (see Fig. 6d), and tiny hysteresis of 5.14% are all achieved by the developed MX/CS pressure sensor (see Fig. 6e). The sensor also offers fast response/relaxation time (52/40 ms) under the applied pressure of 98 kPa (see Fig. 6f). The sensor could identify human activity with a high accuracy of 98.61% with the aid of a deep convolutional neural network [145]. Figure 6a demonstrates the structure of the sensor and also provides the performance data of the sensor in Fig. 6b-f.

4.2.2 Strain sensor

For a strain sensing application, H. Zhang et al. created a self-healing, durable, conductive hydrogel utilizing benzaldehyde-containing polyurethane (VPU), CS, and MX treated with tannic acid (TA). The VPU/CS/TA-MX coating is very ideal for the application in flexible wearable electronic devices because to its promising mechanical and conductivity characteristics. High tensile strength and elongation are demonstrated by the sensor at a break of 5.58 MPa (see Fig. 7b) and 340%, respectively. In the pressure range between 1 to 15 kPa, they have a maximum sensitivity of 0.204 kPa^{-1} and can detect pressures up to 100 kPa. Additionally, evaluated was the sensors' reaction to human knee (see Fig. 7c), elbow (see Fig. 7d), and fingers (see Fig. 7e) movements. Also, the research team observes the performance of the sensor during badminton by analyzing the movement of the wrist (see Fig. 7f-h). The findings showed that the VPU/CS/TA-MX sensors could identify and distinguishing between various human joint motions. They received 60% and 50% of the responses, respectively [146]. In Fig. 7, both the fabrication of the sensor (see Fig. 7 i-iii) and the outcomes of the study (see Fig. 7 a-h) can be noticed.

4.2.3 Humidity sensor

X. Li et al. built a layered humidity sensor using MX, CS, and quercetin, which was inspired by onions. With an exceptional detection range of 1–98% relative humidity (RH) (see Fig. 8c) and a superior response of 317% (see Fig. 8b), as well as an ultrafast response time of 0.75 s and recovery time of 1.6 s (see Fig. 8e) and long-term stability (more than 15 days), the CS-quercetin modified multilayers (MCQMs) inhibit the degradation of MX in the environment. Nonlinear curves were seen under 75% and 98% RH, but the MCQMs displayed linear I-V curves at 33% and 67% RH. It was evident from the decreased current under reverse bias at 98% RH that MCQMs were changing from metallic to semiconductor-like conduction [165]. Construction of the sensor is illustrated in Fig. 8 (i-iii) along with the performance data graphs of the sensor in Fig. 8a-f. Also, in Table 2, we presented the summary of some of the recent studies of MX/CS composites in pressure sensors, strain sensors, and humidity sensors to showcase the recent progress and the potential of the composite in the long run.

4.2.4 Chemical sensor

Chemical detection is also greatly aided by MX-based sensors. X. Wang et al. was reported. an innovative electrochemical sensor for nitrite detection based on a TiO_2-$Ti_3C_2T_X$ MX/Hexadecyl trimethyl ammonium bromide (CTAB)/CS composite atop a Glassy carbon electrode (GCE). The produced TiO_2-$Ti_3C_2T_X$ /CS/CTAB/GCE electrode

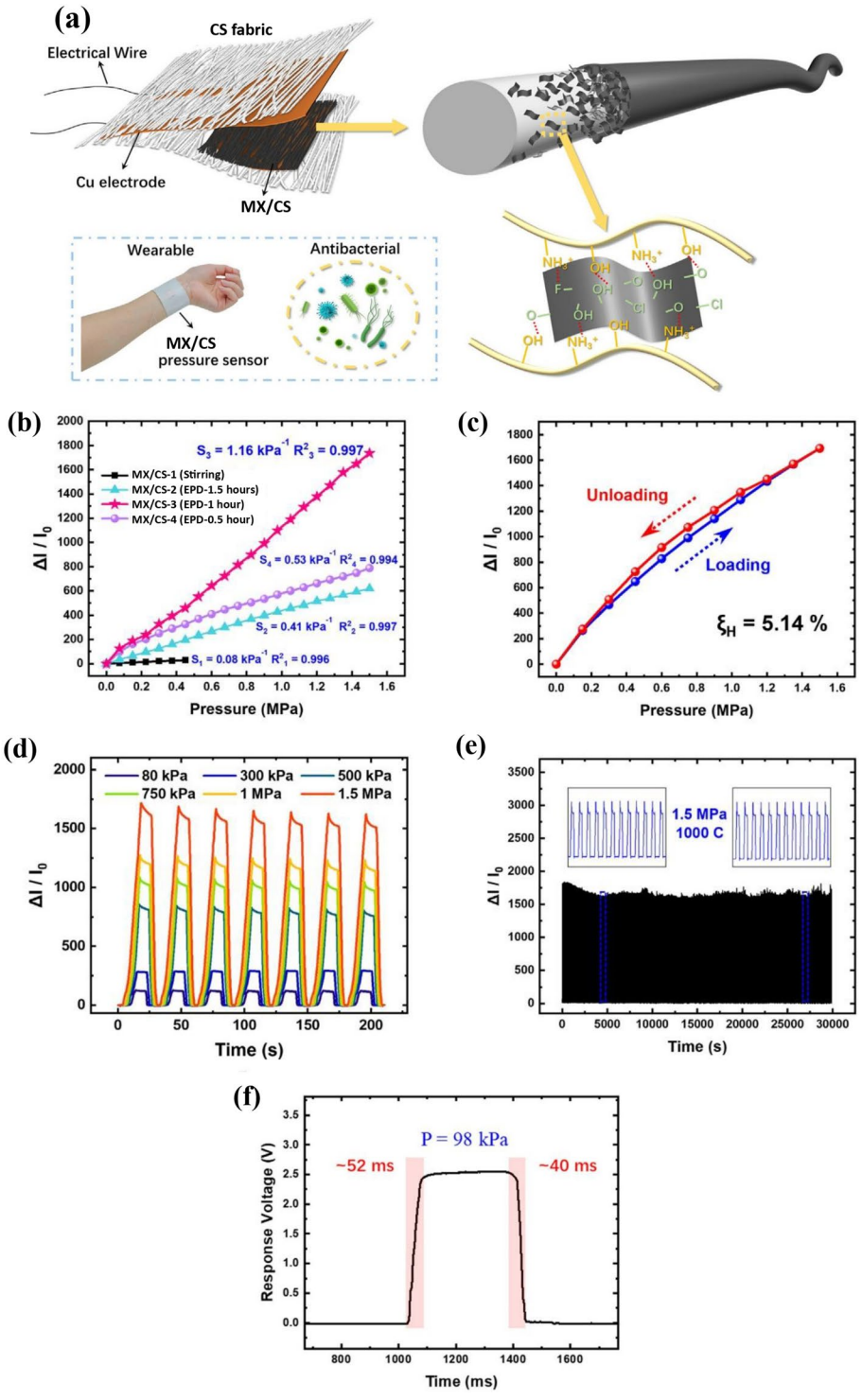

Fig. 6 (a) The fabrication of the MX/CS pressure sensor. (b) Relation between relative current change (ΔI/I0) and pressure. (c) Electrical hysteresis of the pressure sensor. (d) The pressure sensor response over several cycles at various pressures. (e) Durability test. (f) response and recovery time. Published under the CC BY-NC-ND License [145] Copyright 2024, The Authors. Published by Elsevier

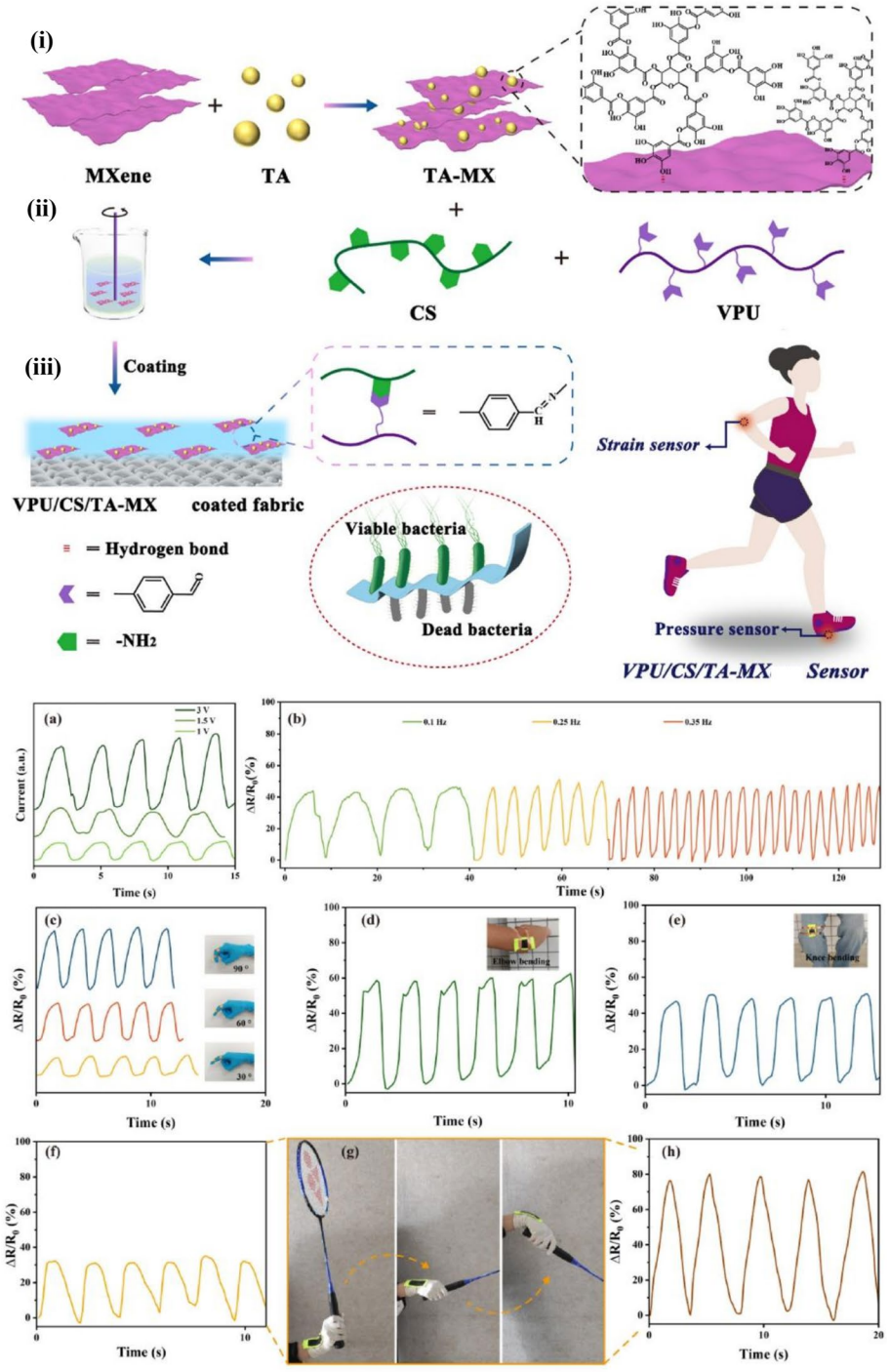

Fig. 7 An illustration of the preparation of a flexible conductive coating. (i) TA monomer-induced hydrogen bonding modification of the conducting ligand MX. (ii) Waterborne aldehyde-based polyurethane synthesis. (iii) The creation of a flexible conductive fabric covering, and the sensing performance (a) Sensor response at various voltages. (b) sensor stretching (10%) response at various frequencies. (c-e) sensor's reaction to knee, elbow, and finger bending. (f-h) sensor's response to wrist monitoring during badminton. Reproduced with permission [146] Copyright 2024, Elsevier

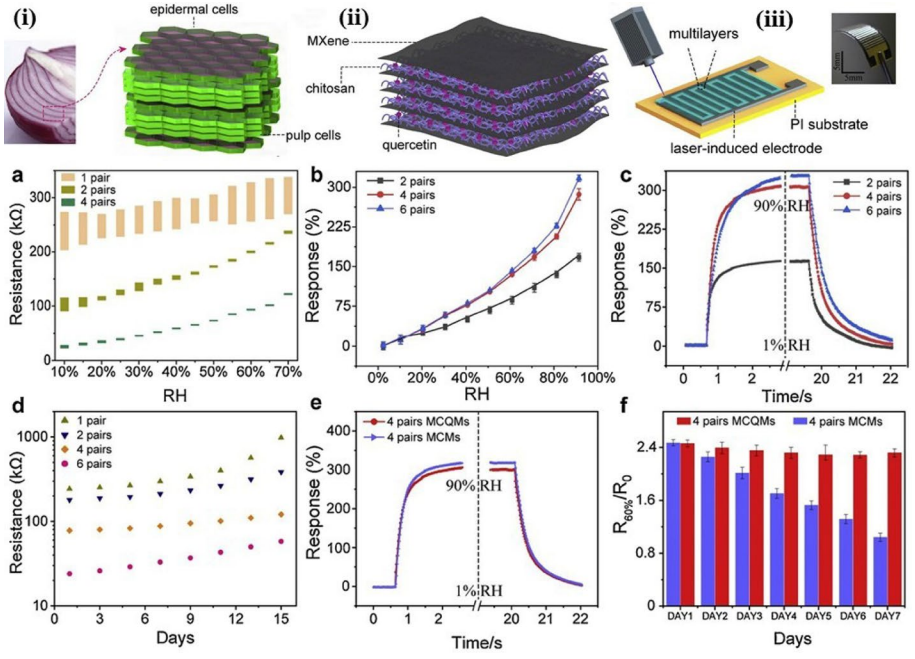

Fig. 8 (i) An illustration and photograph indicating the scale leaves of a purple onion. (ii) MCQMs made of chitosan-quercetin membranes and MXene flakes. (iii) The laser-induced interdigitated electrode on PI substrate serves as the basis for the humidity sensor with a picture of the flexible humidity sensor is included in the inset. Quercetin and multilayer structure effects on humidity sensing; (a–d) Repeatability, sensitivity, response/recovery time, and stability of 1–6 layer-pairs multilayers without quercetin, (e–f) Response/recovery time and stability comparison of multilayers with and without quercetin (MCQMs and MCMs). Reproduced with permission [165] Copyright 2020, Elsevier B.V

showed 2-linear ranges under optimal circumstances. The related linear regression equation was Ip (μA) = 70.4616 c (mM) + 0.0590 (R^2 = 0.9943) for low concentrations between 0.003 and 0.25 mM. The resulting linear regression equation was Ip (μA) = 36.7040 c (mM) + 9.6985 (R^2 = 0.9955) for the high values between 0.25 mM and 1.25 mM. It was determined that the limit of detection (LOD) was 0.85 μM (LOD = 3 × SD/S). High stability (87.8% retention after two weeks), and repeatability (RSD = 1.85%) were all displayed by the sensor. Recoveries of 94–106% were obtained by successful application in actual samples (milk, tap water, and saltwater), which were confirmed by spectrophotometric techniques. [169]. To understand the potential of the MX/CS-based chemical sensors, we highlighted some of the recent studies in Table 3.

4.2.5 Gas sensor

Another area in which MX-based sensors have made great strides is gas detection. Isailović et al. conducted research using CS-stabilized $Ti_3C_2T_X$ MX as an accumulation medium in a disposable, ultrasensitive, and interference-free electrochemical sensor for gaseous H_2O_2 detection. The sensor exhibited exceptionally sensitive and selective electroanalytical performance for detecting trace levels of gaseous H_2O_2, with a very low detection limit of 4 μg/m, a linear response in the concentration range studied of 0.5–30.0 mg/m^3, and strong repeatability with an RSD of 1.3%. The utility of the sensor was demonstrated by the point-of-interest detection of gaseous H_2O_2 using 9% and 12% H_2O_2 solutions during a real hair bleaching procedure [176]. Figure 9(i) represents the notable outcomes of the study by performance analysis graphs (see Fig. 9a-i).

Table 2 A few highlighted examples of MX/CS and MX/CS-hybrid composites and their use of pressure sensing, strain sensing & humidity sensing applications

Sensor type	Medium/Composite	Synthesis method	Sensing performance	References
Pressure sensor	MX/CS	Hierarchical architecture-based fiber by wet-spinning & coating technique	Sensitivity: 1.16 kPa^{-1} Linear range: 1.5 MPa Response Time: 52 ms Recovery Time: 40 ms	[145, 147]
	MX/CMC/C-CNTs	Honeycomb like porous aerogel by freeze drying and crosslinking	Sensitivity: 3.84 kPa^{-1} 0.18 kPa^{-1} Linear range: 0–12.4 kPa 32.8–80.9 kPa Response Time: 62 ms	147
	MX/CS/MC	Hollow bamboo structure aerogel fabricated by physical blending and freeze drying	Sensitivity: 2.90 kPa^{-1} Linear range: 10 kPa Response Time: 119 ms Recovery Time: 91 ms	[148]
	MX/CS/PU@PVP	3D sponge by electrostatic self-assembly	Sensitivity: 50.27 kPa^{-1} 13.3 kPa^{-1} Linear range: 0–7 kPa 7–13 kPa Response Time: 160 ms Recovery Time: 130 ms	[149]
	MX/CS/PU	Flexible sponges fabricated by dip-coating technique	Sensitivity: 0.014 kPa^{-1} 0.18 kPa^{-1} 0.001 kPa^{-1} Linear range: < 6.5 kPa 6.5–85.1 kPa > 85.1 kPa Response Time: 19 ms Limit of detection: 9 Pa	[150]
	MX/CMC-LS/C-CNTs	Porous hydrogel fabricated by freeze drying	Sensitivity: 2.33 kPa^{-1} 1.04 kPa^{-1} 0.53 kPa^{-1} Linear range: 0–10 kPa 10–31 kPa 31–53 kPa Response Time: 140 ms Recovery Time: 60 ms	[151]

Table 2 (continued)

Sensor type	Medium/Composite	Synthesis method	Sensing performance	References
	MX/CMC	Aerogel fabricated by freeze casting and freeze drying	Sensitivity (GF): 6.78 Linear range: ~ 323 kPa Response Time: 87.6 ms Recovery Time: 175 m	[152]
	MX/CS/PEDOT:PSS/PU	A sponge fabricated via dip coating method	Sensitivity: 0.217 kPa^{-1} 0.0093 kPa^{-1} Linear range: 1.8–6.15 kPa 6.15–35 kPa Response Time: 140 ms Recovery Time: 43 ms	[153]
	MX/CS	Elastic 3D aerogel fabricated by freeze drying method	Sensitivity: 709.38 kPa^{-1} 252.37 kPa^{-1} Linear range: < 1 kPa 1–20 kPa Response Time: 116 ms Recovery Time: 112 ms	[154]
	MX/CS-DA	The composite fabricated via dip-coating method	Sensitivity: 15.135 kPa^{-1} Linear range: 0–552.87 kPa Response Time: 0.46 s Recovery Time: 0.47 s	[155]
	MX/CS/PVDF-$BaTiO_3$	Aerogel fabricated by electrospinning and freeze-drying method	Sensitivity: 0.013 V/N Linear range: 10–70 N 1–7 Hz Response Time: < 0.09 s	[156]
	MX/CS/PU	CS modified PU foam coated with MX by 3D printing	Sensitivity: 428.94 kPa^{-1} Linear range: 0–550 kPa Response Time: 75 ms Recovery Time: 60 ms	[157]
Strain sensor	VPU/CS/TA-MX	Flexible fabric coating prepared via TA-MX and CS-VPU fabric then combine them	Tensile strength: 5.58 MPa Stress Limit: 340% Self-healing efficiency: 96%,	[146]
	MX/CS/PVA	A multifunctional hydrogel via one-pot and freeze–thaw cycle methods	Tensile Strength: 3.42 MPa Strain range: 600% Conductivity: 163.15 mS/m Gauge factor (GF): 7.03	[158]

Table 2 (continued)

Sensor type	Medium/Composite	Synthesis method	Sensing performance	References
			Response Time: 42 ms	
	MX/CS/PVA	A tri-network hydrogel prepared via proportionally mixing the components then drying	Tensile Strength: ~ 280 MPa	[159]
			Strain range: ~ 1580%	
			Conductivity: ~ 2.72 S/m	
			Response Time: 0.25 s	
	MX/CS	A conductive aerogel fabricated by freeze drying method	Tensile Strength: 450 Pa	[160]
			Strain range: ~ 99%	
			Detection limit: 1 Pa	
			Response Time: 109.6 s	
			Recovery Time: 110.6 s	
	MX/CS-PA-AA	Hydrogel synthesized by thermally induced polymerization	Tensile Strength: 120.4 kPa	[161]
			Strain range: ~ 918%	
			Conductivity: ~ 1.34 S/m	
			Gauge factor (GF): 3.94	
			Response Time: 0.25 s	
	MX/PAA-CS	A double network hydrogel was fabricated adapting gel immersion technique	Tensile Strength: 3.3 kPa	[133]
			Strain range: 746.2%	
			Conductivity: 0.8–1.8 S/m	
			Gauge factor (GF): 11.70	
	IL-MX/CS/PAM/PAA	The fabrication method involves in-situ free radical polymerization and UV curing	Tensile Strength: 1050 kPa	[162]
			Strain range: 2980%	
			Gauge Factor: 4.2–13.6	
			Response Time: 200 ms	
	MX/CS/PAM	The fabrication method involves in-situ free radical polymerization	Tensile Strength: 70.6 kPa	[163]
			Strain range: 2800%	
			Gauge Factor: 3.24	
			Response Time: 300 ms	
			Recovery Time: 300 ms	
	AMS-MX/CS/VPA	The film was fabricated by solution casting method	Tensile Strength: 0.127 MPa	[144]
			Strain range: 550%	
	MX/OSA-CS	The hydrogel formed via multi-dynamic interactions	Tensile Strength: 0.91 MPa	[164]
			Strain range: 820%	
			Gauge Factor: 11	
			Response Time: 9.6 s	
			Recovery Time: 2.6 s	
Humidity Sensor	MX/CS/QC	A multilayer membrane fabricated by layer-by-layer assembling technique	Detection range: 1–98% RH	[165]
			Sensitivity: 317% at 90% RH	
			Response Time: 0.75 s	
			Recovery Time: 1.6 s	

Table 2 (continued)

Sensor type	Medium/Composite	Synthesis method	Sensing performance	References
	MX/CS-TPU	The sensing layer was prepared by electrospinning of CS-TPU followed by a dip coating of MXene	Detection range: 11–94% RH	[166]
			Hysteresis: < 7% RH	
			Response Time: 12–16 s	
			Recovery Time: 30–32 s	
	NCN/MX/CS-QCM	The sensor prepared by ultrasonic mixing of NCN-MXene followed by drop coating on QCM	Detection range: 11.3–97.3% RH	[167]
			Hysteresis: 2.12% RH	
			Response Time: 4.4 s	
			Recovery Time: 4.1 s	
	MX/CS/PVDF	Aerogel prepared via vacuum freeze drying	Detection range: ~ 98% RH	[168]
			Hysteresis: 3.2% RH	
			Response Time: 6 s	
			Recovery Time: 12.5 s	
	MX/CS	Well aligned Film prepared by Vacuum assisted filtration	Detection range: 14–73% RH	[129]
			Sensitivity: ~ 0.16% at 73% RH	
	MX/CS	The film is fabricated by freeze-drying method	Detection range: 11–95% RH	[15]
			Hysteresis: < 6% RH	
			Response Time: 25.6 s	
			Recovery Time: 9.7 s	

GF: Gauge Factor, CMC: Carboxymethyl Chitosan, C-CNT: Carboxylated carbon nanotubes, MC: Methylcellulose, PU: Polyurethene, PVP: Polyvinyl pyrrolidone, LS: Lignosulfonate sodium. VPU: Benzaldehyde-containing polyurethane, TA: Tannic Acid, PVA: Polyvinyl Alcohol, PA: Polyacrylamide, AA: Acrylic acid, NCN: Nanochitin, QC: Quercetin, TPU: Thermoplastic polyurethane, QCM: Quartz crystal microbalance, PVDF: Polyvinylidene difluoride, CS-DA: Chitosan-modified Polyester-spandex knitted fabric, PAA: Polyacrylic acid, PAM: Polyacrylamide, IL-MXene: Ionic liquid-MXene, VPA: Vanillin-polyacrylate, AMS-MXene: Mesoporous nanosilica-MXene, OSA: Oxidized Sodium alginate

4.2.6 Metal ion sensor

MX/CS electrodes have recently emerged as a viable substitute for conventional ones, offering benefits such as superior resolution of nearby peaks and environmental friendliness. X. Hu et al. reported using MXene/carboxymethyl CS (CMC) nanochannels to detect and identify copper ions with great sensitivity. With sufficient space charges, CMC amplifies the nanochannel's nanoconfinement effect. Crucially, the MX/CMC has the capacity to detect Cu^{2+} because the CMC can chelate with Cu^{2+} ions. The current signal varies noticeably because of the space charges being reduced by the development of CMC-Cu^{2+} complexes. Therefore, considering the characteristics of the nanochannel composition, MX/CMC can accomplish very sensitive and stable Cu^{2+} detection. Cu^{2+} detection has a low detection limit of 0.095 nM and a linear response range of 10^{-9} to 10^{-5} M. Interestingly, MXene/CMC was effectively used to detect Cu^{2+} in blood samples from fetal bovines and actual water [177]. In Fig. 10, the fabrication (see Fig. 10a) and the working mechanism (see Fig. 10b) of the metal ion sensor are shown by simple illustration.

Table 3 A few highlighted examples of MX/CS and MX/CS-hybrid composites and their applications as chemical sensors

Medium/Composite	Synthesis method	Target analyte	Method pf detection	Sensing performance	References
TiO_2-MX/CS/CTAB	The TiO_2-MX/CS/CTAB coated GCE prepared by two-step calcination method	Nitrite	Differential pulse voltammetry	Detection Limit: 0.85 mM	[169]
				Linear range: 0.003–1.25 mM	
				Linearity: 0.9955	
				Recoveries: 94–106%	
PGOx/MX/CS	The nanocomposite is prepared by electrostatical assembly	Glucose	Differential pulse voltammetry	Detection Limit: 3.1 mM	[143]
				Linear range: 0.03–16.5 mM	
				Sensitivity: 48.98 mA/M.cm	
MX/CS/NiCo-LDH	The composite fabricated by layer-by-layer assembly followed by CS coating	Glucose	Differential pulse voltammetry	Detection Limit: 0.21 mM	[170]
				Linear range: 1 m–3.998 mM	
				Sensitivity: 154.05 $mAmM^{-1}.cm^{-2}$	
MX/CS/Cu_2O	The electrode prepared through electrostatic interaction and electrodeposition	Glucose	Cyclic voltammetry	Detection Limit: 52.4 mmol/L	[171]
				Linear range: 52.4–2000 mmol/L	
				Sensitivity: 60.295 $mA.L/mmol.cm^2$	
				Recoveries: 98–100%	
MX/CS/Cu_2O	The electrode prepared through electrostatic interaction and electrodeposition	Cholesterol	Cyclic voltammetry	Detection Limit: 49.8 mmol/L	[171]
				Linear range: 49.8–200 mmol/L	
				Sensitivity: 215.71 $mA.L/mmol.cm^2$	
				Recoveries: 98–102%	
MX/AChE-CS/AuNP/MOF	The mixture coated of GCE and stored in refrigerator (4 °C) for drying	Methamidophos (Pesticide)	Cyclic voltammetry & Differential pulse voltammetry	Detection Limit: 1.3×10^{-13} M	[172]
				Linear range: 10^{-12}–10^{-6} M	

Table 3 (continued)

Medium/Composite	Synthesis method	Target analyte	Method pf detection	Sensing performance	References
				Sensitivity: 0.005–4 mM Recoveries: 95.2–101.3%	
Tyr/MX/CS/GCE	The Tyr/MX/CS solution prepared and simply casted onto GCE then dried at 4 °C	Phenol	Ampero-metry	Detection Limit: 12nM	[173]
				Linear range: 0.05–15.5 mM Sensitivity: 414.4 mA/M Recoveries: 95.2–101.3%	
PM/MX/CS	A film fabricated through electrostatically mediated layer-by-layer (LBL) self-assembly	L-tryptophan	Differential pulse voltammetry	Detection Limit: 0.08 µM	[174]
				Linear range: 0.1–103 µM Linearity: 0.995 Sensitivity: 0.141 µA/ µM.cm^2 Recoveries: 95.78–104.31%	
MX/CMC	A film fabricated through solution blending and film casting method	Ciprofloxacin	Cyclic voltammetry	Detection Limit: 0.003 µM	[175]
				Linear range: 0.1–20 µM Linearity: 0.9997 Sensitivity: 0.0527 µA/ µM Recoveries: 96.2–104.2%	

PGOx: Glucose oxidase polynanogel, AuNP: Gold Nanoparticle, MOF: Metal organic framework, AChE: Acetylcholinesterase, Tyr: Tyrosinase, NiCo-LDH: Nickel-cobalt layered double hydroxide, CMC: Carboxymethyl Chitosan, PM = Polyoxometalate

4.3 Wastewater treatment

Composite materials of MX and CS are becoming increasingly effective filtering materials for eliminating a wide range of pollutants, including salts (for desalination), dyes, heavy metals, radionuclides, and pharmaceutical residues. The synergistic qualities of CS (biocompatibility, chelation ability, and film-forming capabilities) and MXs (conductivity, large surface area, and functional groups) account for their efficacy [1]. MX/CS composites primarily function through adsorption, where pollutants are attracted to the surface of the material via electrostatic interactions. The negatively charged surface of MX attracts cationic pollutants, such as heavy metals, through hydrogen bonding and chelation, where metals and organic pollutants are bound by the -NH_2 and -OH groups of CS. Hydrophobic interactions and π-π stacking, in addition to natural dyes and pharmaceutical residues, are further factors considered [64, 178, 179]. The sieving effect and

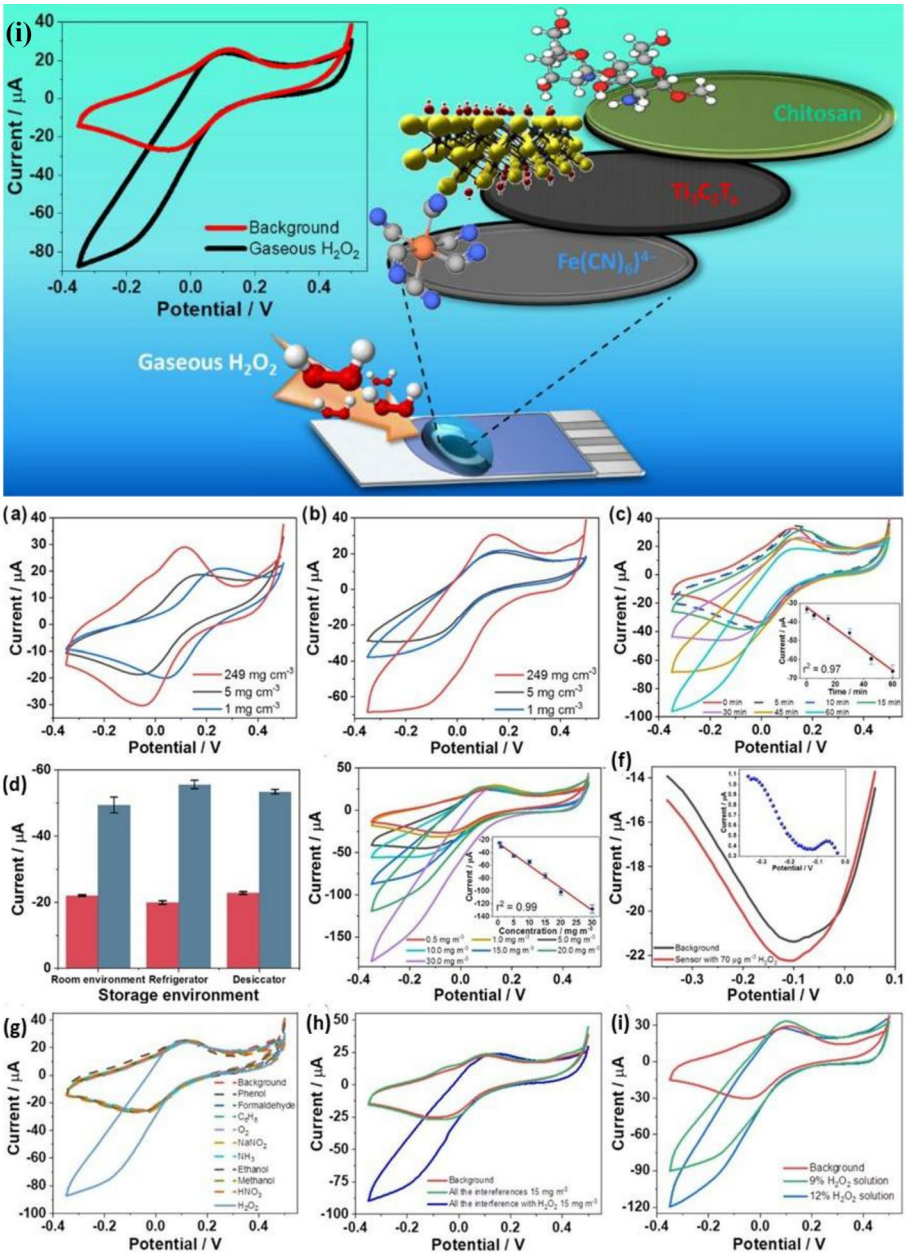

Fig. 9 (i) Illustration of detection of H_2O_2 by $Ti_3C_2T_x$ MX/CS gas sensor; (a-f) Electroanalytical Performance of the sensor; (g-i) Selectivity Study of the sensor. Published under CC-BY License [176] Copyright 2023, The Authors. Published by the American Chemical Society

size exclusion are two other popular methods for removing or separating contaminants. Larger molecules, such as certain dyes and pharmaceutical pollutants, can be physically blocked by membranes composed of the MX/CS composite, which have adjustable pore widths. The 2D layered structure of MX forms nanochannels that trap impurities while allowing water to pass through selectively [180, 181]. One of the intriguing characteristics that makes MX particularly appealing to researchers is its photocatalytic properties. Under light, MXs (such as $Ti_3C_2T_X$) exhibit photocatalytic activity, degrading metal ions and organic contaminants, including methylene blue, tetracycline, and salts. Photocatalysts based on MX have shown great promise for eliminating emerging pollutants due to

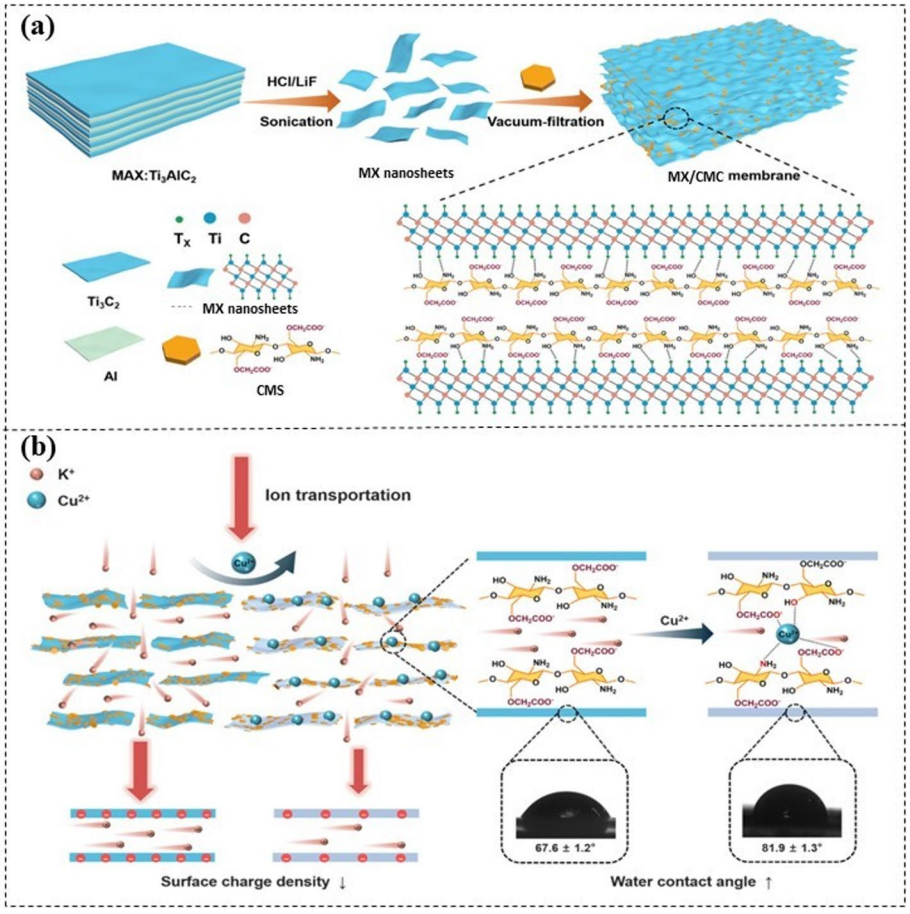

Fig. 10 (a) An illustration of MX/CMC nanochannel fabrication, (b) the detection mechanism of Cu^{2+} ions from water. Reproduced with permission [177] Copyright 2024, Royal Society of Chemistry.

their unique properties. These characteristics include an extensive surface region, high electrical conductivity, and a shifting surface chemistry [182, 183].

4.3.1 Dye removal

R Wang et al. uses a simple hydrothermal and self-assembly method to create a novel magnetic adsorbent with $CoFe_2O_4$/CS supported onto alkalized MX (alk-MX) for the removal of dyes such as Congo Red (CR), Rhodamine B (RhB), and Malachite Green (MG). The addition of $CoFe_2O_4$/CS to alk-MX can significantly enhance the adsorption capacity for cationic and anionic dyes, as indicated by batch investigations on the adsorption of CR, RhB, and MG dyes. For CR, RhB, and MG dyes, respectively, an ultra-high adsorption capacity of up to 2095.9, 1333.9, and 537.6 mg/g is attained. The experiment was conducted for 2 hours at 25 °C, with a pH range of 2–12, and the initial concentration of the sample was 20 mg/L. The overall percentage of elimination was between 97 and 99% [184]. The Fabrication process (see Fig. 11a) and the working mechanism (see Fig. 11b) of the membrane to eliminate dyes from wastewater can be seen in Fig. 11.

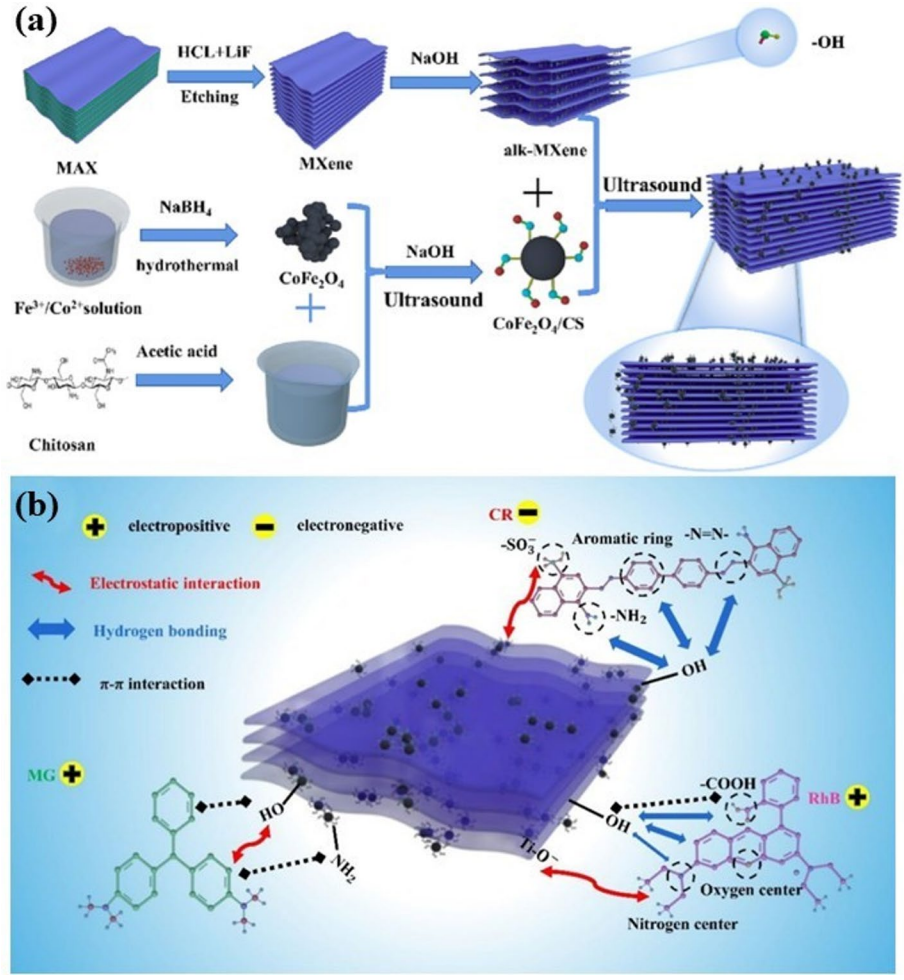

Fig. 11 (a) The hydrothermal synthesis of alk-MX/CS/CoFe2O4 medium, (b) the removal mechanism of CR, MG, and RhB dyes from aqueous medium. Reproduced with permission [184] Copyright 2023, Elsevier B.V

4.3.2 Metal ion removal

In a study, by modifying the Ti_3C_2 MX and CS composite with disodium ethylenediaminetetraacetate (EDTA·2Na) agent, Qiang et al. was able to effectively create a new adsorbent for the removal of hexavalent chromium (Cr (VI)) in aqueous solution (see Fig. 12). The adsorption rate of the experiment was 124.76 mg/g, and its removal efficiency of Cr (VI) was 100%. Solutions of Cr (VI) at several concentrations (25–100 mg/L) were prepared. The experiment was conducted for 2 h, maintaining a pH level between 1 and 9, with maximum adsorption occurring at pH 2. The temperature range for the experiment was 298–338 K [185]. The fabrication method of the MX/CS composite shown in Fig. 12a and the performance data can be found in Fig. 12b-d. In order to represent the potentials and efficiency of the MX/CS filtration system for heavy metals and dye removal, we highlighted some recent research in Table 4.

4.3.3 Pharmaceutical pollutant removal

To eliminate the pharmaceutical pollutants (norfloxacin and ciprofloxacin) from aqueous solution, Bukhari et al. designed a ternary composite of CS and MX functionalized graphene oxide (MX/CS/GO) based on anion-synergistic interaction (see Fig. 13a). The

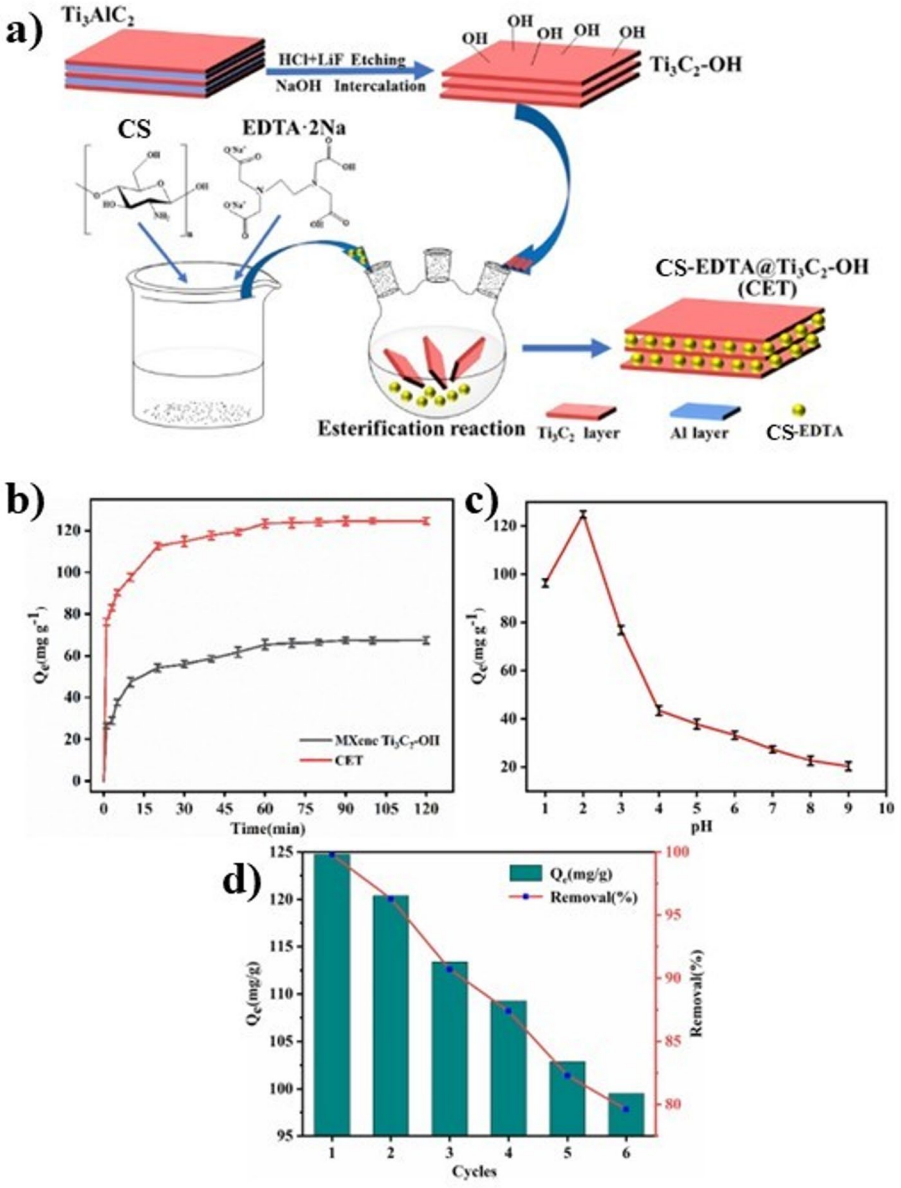

Fig. 12 (a) Schematic representation of EDTA modified Ti_3C_2 MX/CS composite. (b) Adsorption performance and efficiency over time. (c) Effect of pH on adsorption efficiency. (d) Removal percentage over 6-cycles of operations. Reproduced with permission [185] Copyright 2023, Elsevier Ltd and Techna Group S.r.l

study discovered that the MX/CS/GO composite had exceptional adsorption capacities for ciprofloxacin and norfloxacin at 328 K, with respective values of 7.53 mmol/g and 4.75 mmol/g, and a broad pH range (2–12). During the first cycle of the 60-min trial, the clearance rates of both ciprofloxacin and norfloxacin were 100% (see Fig. 13b-c). Remarkably, both norfloxacin and ciprofloxacin had clearance efficiencies of greater than 95% even after three cycles [200]. Table 5 highlights some of the studies involving the MX/CS system to eliminate pharmaceutical pollutants from wastewater; the table provides some additional insights about the potential of the composite.

Table 4 A few highlighted studies of MX/CScomposites and their applications for the removal of dye and metal ions from wastewater

Medium/Composite	Synthesis method	Pollutant	Process parameters	Removal performance	References
alk-MX/CS/$CoFe_2O_4$	The composite synthesized via through a hydrothermal and self-assembly method	CR,	Temp: 25 °C	Capacity:	[184]
		RhB,	Time: 2 h	CR: 2095.9 mg/g	
		MG	pH: 2–12	RhB: 1333.9 mg/g	
			Initial Conc.: 20 mg/L	MG: 537.6 mg/g	
				Removal: 97–99% (Overall)	
MX/CS/ZnS/CL	The catalytic composite synthesized centrifuge mixing & drying method	AR80	Temp: 25 °C	Capacity:	[186]
		EBT	Time: 6 h	1.29 g/g *(Adsorp.)*	
		MB	pH: 3–10	5.63 g/g *(Adsorp + Photodegradation)*	
			Initial Conc.: 50 mg/L	Removal: ~ 100% (Overall)	
MX/CS/MOF	The composite fabricated via centrifuge dispersion & drying	MB	Temp: 25 °C	Capacity: ~ 425 mg/g	[187]
			Time: 1 h		
			pH: 2–9		
			Initial Conc.: 400 mg/L		
MX/CS/GO	The catalytic nanocomposite-based membrane was fabricated by casting method	MB	Temp: 25 °C	Removal: 96%	[188]
			Time: 8 h		
			Initial Conc.: 20 mg/L		

Table 4 (continued)

Medium/Composite	Synthesis method	Pollutant	Process parameters	Removal performance	References
MX/CS-PCM	The pod-inspired composite synthesized via assemble the components and casting method	CV	Temp: 25 °C	Capacity: 2,750 mg/g	[189]
			Time: 12 h pH: 4–10 Initial Conc.: 400 mg/L	Removal: 100%	
MX/CS/Fe_3O_4	The magnetic composite fabricated via ultrasonic mixing/dispersion followed by casting	CR	Temp: 25 °C	Capacity: 620.22 mg/g	[190]
			Time: 5 h pH: 6–13 Initial Conc.: 45 mg/L		
MX/CS/PAN	The film fabricated via vacuum filtration and electrospinning	AB, SR, CBB, CR, MB	Temp: 25 °C Pressure: 0.2 MPa Initial Conc.: 100 mg/L	Removal: AB: 99.83% SR: 99.04% CBB: 99.93% CR: 98.84% MB: 54.28% Flux (L/m^2h): AB: 435.23 SR: 244.71 CBB: 573.76 CR: 505.11 MB: 1279.91	[191]
MX/CTNC/TiO_2	The membrane fabricated via vacuum filtration on a polydopamine base	MeB CR CV	Temp: 30 °C Time: 30 min pH: 8.5	Removal: MeB: 93.80% CR: 97.08% CV: 98.90%	[68]

Table 4 (continued)

Medium/Composite	Synthesis method	Pollutant	Process parameters	Removal performance	References
MX/CS/PAN	The membrane fabricated via vacuum filtration nethod	CR	Time: 12 h	Removal: > 99%	[192]
			Temp: 25 °C Pressure: 0.1–0.8 Mpa Initial Conc.: 100 mg/L	Flux (L/m^2h): 715.3	
alk-MX/CMS	The individual components assembled then the composite synthesized by chemical cross-linking method	Cr^{6+}	Temp: 25–55 °C	Capacity: ~ 125 mg/g	[185]
			Time: 2 h pH: 1–9 Initial Conc.: 25–100 mg/L	Removal: 100%	
MX/CS/LS/Fe_3O_4	The magnetic composite is prepared by freeze drying and oven drying method	Cr^{6+}	Temp: 25 °C	Capacity: 42.5 mg/g	[193]
			Time: 6 h pH: 2–8 Initial Conc.: 30 mg/L	Removal: 90%	
MX/CS-IMIZ	The composite was synthesized by in situ Radziszewski reaction	Cr^{6+}	Temp: 25 °C	Capacity: 183.8 mg/g	[194]
			Time: 1.25 h pH: 1–8 Initial Conc.: 30 mg/L	Removal: ~ 95%	
MX/CS	The composite fabricated by vacuum drying	Cr^{6+}	Temp: 25 °C	Capacity: 16.1 mg/g	[195]
			Time: 24 h pH: 2–7 Initial Conc.: 100 mg/L	Removal: ~ 40.5%	

Table 4 (continued)

Medium/Composite	Synthesis method	Pollutant	Process parameters	Removal performance	References
MX/CS	The composite was prepared by simple assembly (mixing) and oven drying	Zn^{2+}	Temp: 25 °C	Capacity:	[196]
		Cd^{2+}	Time: 60 min pH: 2–10 Initial Conc.: 5–100 mg/L	93.47 mg/g (Zn^{2+}) 79.66 mg/g (Cd^{2+}) Removal: 100% (Zn^{2+}) 100% (Cd^{2+})	
MX/CS/MOF	The composite fabricated via centrifuge dispersion & drying	Pb^{2+}	Temp: 25 °C	Capacity: 448.93 mg/g	[187]
			Time: 49 min pH: 3–6 Initial Conc.: 400 mg/L	Removal: 90%	
MX/CS/GO	The catalytic nanocomposite-based membrane was fabricated by casting method	Co^{2+}	Temp: 25 °C	Removal:	[188]
		Cu^{2+}	Time: 8 h Initial Conc.: 20 mg/L	78% (Co^{2+}) 76% (Cu^{2+})	
MX/CS	The composite modified with KH_2PO_4 by heat treatment	Cs^{+}	Temp: 25 °C	Capacity: 338.75 mg/g	[197]
			Time: 1 h pH: 3–11 Initial Conc.: 150 mg/L		
MX/CS/LS	The membrane prepared by solution casting method	Cu^{2+}	Temp: 20 °C	Capacity:	[64]
		Pb^{2+} Cr^{6+} Ni^{2+}	Time: 2 h pH: optimal Initial Conc.: 5–500 mg/L	Cu^{2+}: 9 mg/g Pb^{2+}: 9.8 mg/g Cr^{6+}: 8.0 mg/g	

Table 4 (continued)

Medium/Composite	Synthesis method	Pollutant	Process parameters	Removal performance	References
		Co^{2+}		Ni^{2+}: 6.0 mg/g Co^{2+}: 5.5 mg/g Removal: Cu^{2+}: 90% Pb^{2+}: 98% Cr^{6+}: 80% Ni^{2+}: 60% Co^{2+}: 55%	
MX/CS/PUF	The membrane prepared by dip-coating method	Cr^{6+}	Temp: 25 °C Time: 4 h pH: 2–6 Initial Conc.: 10–50 mg/L	Removal: ~ 70%	[198]
MX/CS/Fe_3O_4	The 3D network foam fabricated via self assembly technique	Cr^{6+}	Temp: 25 °C	Capacity:	[199]
		U^{6+}	Time: 24 h pH: 1–8 Initial Conc.: 0–20 mg/L	Cr^{6+}: 83.1 mg/g U^{6+}: 106.2 mg/g	

alk: alkalized, CL: Cellulose, MOF: Metal organic framework, GO: Graphene oxide, CS-PCM: Chitosan-based porous carbon microspheres, CMS: Carboxylated chitosan, LS: Lignosulfonate, PUF: Polyurethane, IMIZ: Polyimidazoles, PAN: Polyacrylonitrile, CTNC: Chitin Nanocrystal, LS: Lignosulfonate, CR: Congo Red, RhB: Rhodamine B, MG: Malachite Green, AR80: Acid Red 80, EBT: Eriochrome Black T, MB: Methyl Blue, CV: Crystal Violet, AB: Alcian blue 8GX, SR: Sirius red, CBB: Coomassie brilliant blue, MeB: Methylene Blue

Cr^{6+}: Chromium (VI) ion, Zn^{2+}: Zinc (II) ion, Cd^{2+}: Cadmium (II) ion, Pb^{2+}: Lead (II) ion, Co^{2+}: Cobalt (II) ion, Cu^{2+}: Copper (II) ion, Cs^{+}: Cesium ion, U^{6+}: Uranium (VI)

4.3.4 Oil/water separation

In a research study by Z. Wu et al., a method of CS-aided MX assembly onto polymer fabric (CMF) is used to create a high efficiency solar-driven interfacial evaporation (SDIE) of oil-contaminated saltwater, which possesses a super-hydrophilic and flexible nature. With an efficiency of 88.05% under one sun light and a high evaporation rate of 1.50 kg/m^2h, the CMF functions as a solar absorber and a water transporter in an evaporation device. Water droplets may diffuse and penetrate the fabric in just 26 ms because of the remarkable superhydrophilicity of CMF. With the CMF attaining a water-pumping height of 67 mm instead of 49 mm for the immaculate fabric, this characteristic allows for adequate water transportation. When pre-wetted, the CMF may efficiently resist crude oil, according to experiments, which makes it appropriate for areas damaged by oil. Low levels of total organic carbon (TOC) in the condensate indicate that the evaporator evaporated almost all oil and surfactants, achieving an evaporation rate of approximately 1.52 kg/m^2h. While dry CMF needed heat to lower oil viscosity before water contact, pre-wetted CMF quickly repelled oil and started evaporation in crude oil-contaminated saltwater. The CMF's durability and performance were validated in outdoor tests, producing 5.7–8.6 L/m^2day fresh water. Its superhydrophilicity and porous

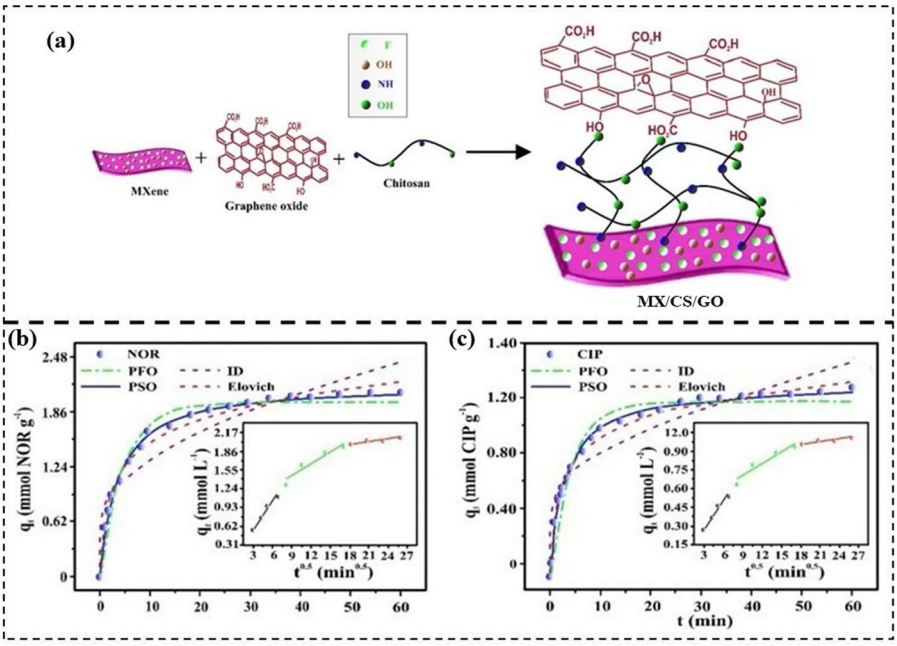

Fig. 13 (a) An illustration of MX/CS/GO composite fabrication and removal efficiency of (b) Norfloxacin and (c) Ciprofloxacin by MX/CS/GO composite. Reproduced with permission [200] Copyright 2023, Elsevier B.V

structure facilitate rapid water transport and salt rejection, preventing salt accumulation. The CMF maintained stable performance over 24 cycles and in high-salinity (20 wt%) seawater. Outdoor experiments confirmed the effectiveness and durability of CMF, yielding 5.7–8.6 L/m^{2}day of fresh water. Its porous structure and superhydrophilicity allow quick water transfer and salt rejection, stopping salt buildup. In high-salinity (20 weight percent) saltwater, the performance of CMF remained consistent throughout 24 cycles [205]. Figure 14a-f provides a visual understanding of the success of this study.

4.4 Supercapacitor

A supercapacitor is a device that stores electrical energy but has a significantly quicker rate of charge and discharge. Pseudocapacitance is another technique used by certain supercapacitors to improve charge storage through electrochemical processes on the electrode surface [206–208]. Due to their large surface areas and excellent electrical conductivity (~10,000 S/cm), MXs are utilized in supercapacitors. Studies demonstrate high volumetric capacitance (e.g., $Ti_3C_2T_x$-based symmetric supercapacitors achieving energy densities above 41.3 mWh/cm^3 at 1.8 V), highlighting their importance in both electric double-layer capacitance and pseudocapacitance [4, 209, 210]. CS offers a sustainable alternative to conventional materials, such as hazardous polymers, and is utilized in the development of electrodes, electrolytes, and binders. The high ionic conductivity (e.g., 2.59×10^{-2} S/cm) and mechanical robustness of CS-based hydrogels as an electrolyte make them suitable for flexible supercapacitors that operate over a wide temperature range (– 11 to 70 °C) [211–213].

A 3D ordered and porous $Ti_3C_2T_x$ MX and CS film was developed for high rate pseudocapacitive energy storage in a work by Y. Ding et al. With a high mass loading of 4mg cm^{-2}, the $Ti_3C_2T_x$ MX/CS film exhibits 57.1% capacitance retention, achieving a 400-fold increase in scan rate, and delivers a capacitance of 245.2 F/g at 2 V/s. Additionally,

Table 5 A few highlighted studies on MX/CS and MX/CS-hybrid composites, as well as their applications in removing pharmaceutical pollutants from wastewater

Medium/Composite	Pollutant	Process parameters	Removal performance	References
MX/CS/GO	Norfloxacin (NOR)	Temp: 55 °C	Capacity:	[200]
		Time: 1 h	NOR: 7.53 mmol/g	
		pH: 2–12	CIP: 4.75 mmol/g	
	Ciprofloxacin (CIP)		Removal:	
			NOR: 100%	
			CIP: > 95%	
MX/CS/MnO_2	Caffeine	Temp: 25 °C	Removal: 99.9%	[201]
		Time: 6 h	Flux Recovery: 98.6%	
		pH: 4–13	Permeability: 19.33	
		Pressure: 7 Bar	$Lm^{-2}\ h^{-1}\ bar^{-1}$	
MX/CS/PEI	Chlortetracycline (CTC)	Temp: 30–40 °C	Removal:	[202]
		Time: 2 h	CTC: 91.1%	
	Ibuprofen (IBU)	pH: 3–10	IBU: 99.25%	
MX/CS/Co/PMS	Tetracycline	Time: 1 h	Removal: 100%	[203]
		pH: 4–11	Deg. Rate: 0.144 min^{-1}	
MX/CS/C_3N_4	Ofloxacin	Temp: 25 °C;	Removal: 93.5%	[204]
		Time: 1.5 h;		
		Conc.: 10 mg/L		
		Photocatalyst: 50 mg		
MX/CS	Paracetamol (PC)	Temp: 25 °C	Removal:	[65]
	Ibuprofen (IB)	Time: 20 min	IB: 73.8–82.8%	
		pH: 4–13	PC: 61.4–74.6%	
		Initial Conc.: 1–5 ppm		
LC-MX/CS			Removal:	
			IB: 92.8–98.9%	
			PC: 79.3–92.8%	
MnO_2/MX/CS			Removal:	
			IB: 88.8–98.4%	
			PC: 77.2–90.8%	

GO: Graphene Oxide, PEI: Polyethyleneimine, Co: Cobalt, PMS: Peroxomonosulfate, LC-MX: Laccase-coated MXene

an ultra-high power density of 143.2 μWh cm^{-2} can be achieved by assembling flexible symmetrical supercapacitors using a $Ti_3C_2T_x$ MX/CS film. 94% of the outer surface charge is stored in the $Ti_3C_2T_x$ MX/CS electrode, which has a realistic total charge storage of 340 C/g. On $Ti_3C_2T_x$ MX/CS, a high capacitance retention of 95.8% and a coulmbic efficiency (CE) of 99.2% are achieved. The $Ti_3C_2T_x$ MX/CS electrode has an internal resistance of 1.62 Ω [214]. The fabrication method of MX/CS film (see Fig. 15a) and the supercapacitance performances of the composite are shown in Fig. 15b-e. Also, take a look at Table 6, where we compile some of the recent works of MX/CS composites in supercapacitors are highlighted.

4.5 Battery

Electrochemical energy storage is considered a more desirable energy storage solution than traditional fossil fuel-based systems due to its reliability and environmental friendliness [222]. MXs are utilized as electrodes, conductive binders, and in composites for battery applications, enhancing performance in various systems. According to research on thick electrode designs, MXs can act as conductive binders for silicon anodes in lithium-ion batteries, allowing for high areal capacities of up to 23.3 $mAhcm^{-2}$[223, 224]. Moreover, MXs are being investigated for use as cathodes or substrates in aqueous

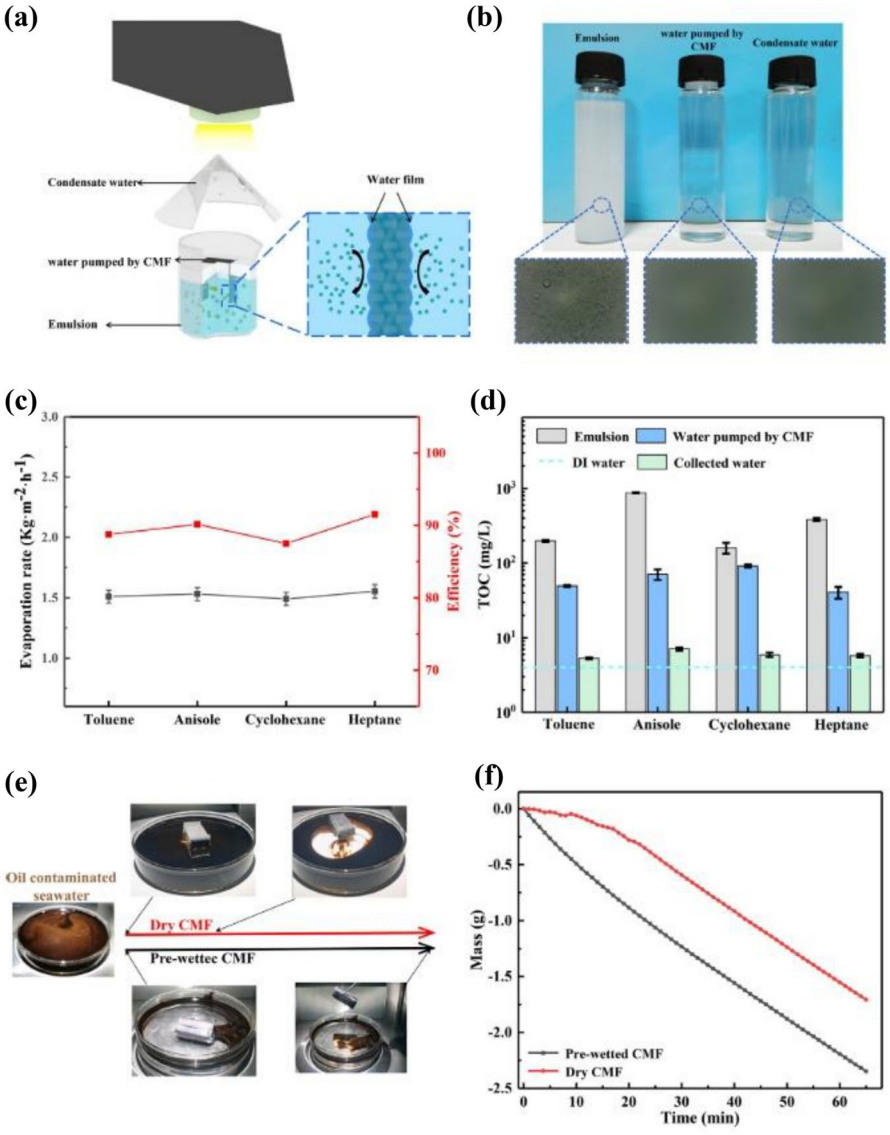

Fig. 14 (a) An illustration of the SDIE of the emulsion. (b) photographs and optical microscope pictures. (c) The efficiency and rate of evaporation of the emulsion while employing the CMF solar absorber. (d) Water pumped from the emulsion via the CMF, total organic carbon content in the emulsion, and collected condensate water from the SDIE. (e) Images and (f) the evaporation property of the saltwater polluted by crude oil utilizing the dry CMF and the CMF that has been pre-wetted with water. Reproduced with permission [205] Copyright 2022, Elsevier

zinc-ion batteries (AZIBs) and multivalent metal-ion batteries (MMIBs), such as those for magnesium and aluminum, providing both safety and cost-effectiveness [225]. With a remarkable 80% capacitance retention rate after 900 cycles, MMIBs exhibit a capacity of nearly 490 mAh/g at a specific current [226]. AZIBs exhibit a exceptional capacitance retention rate of 96.2% after 20,000 cycles, with a capacity of up to 500 mAh/g at a specific current [227]. Research suggests that it can achieve high energy densities and rate capabilities, although there are still issues to be resolved, such as managing surface terminations [228, 229]. The application of CS, particularly in lithium-ion, zinc-ion, and lithium-sulfur batteries, serves as an electrolyte, binder, and additive for gel polymers. CS functions as a polysulfide trapping agent in lithium-sulfur batteries, increasing cycle life and discharge capacity from 950 to 1145 mAh/g at C/10 [230, 231]. By stabilizing

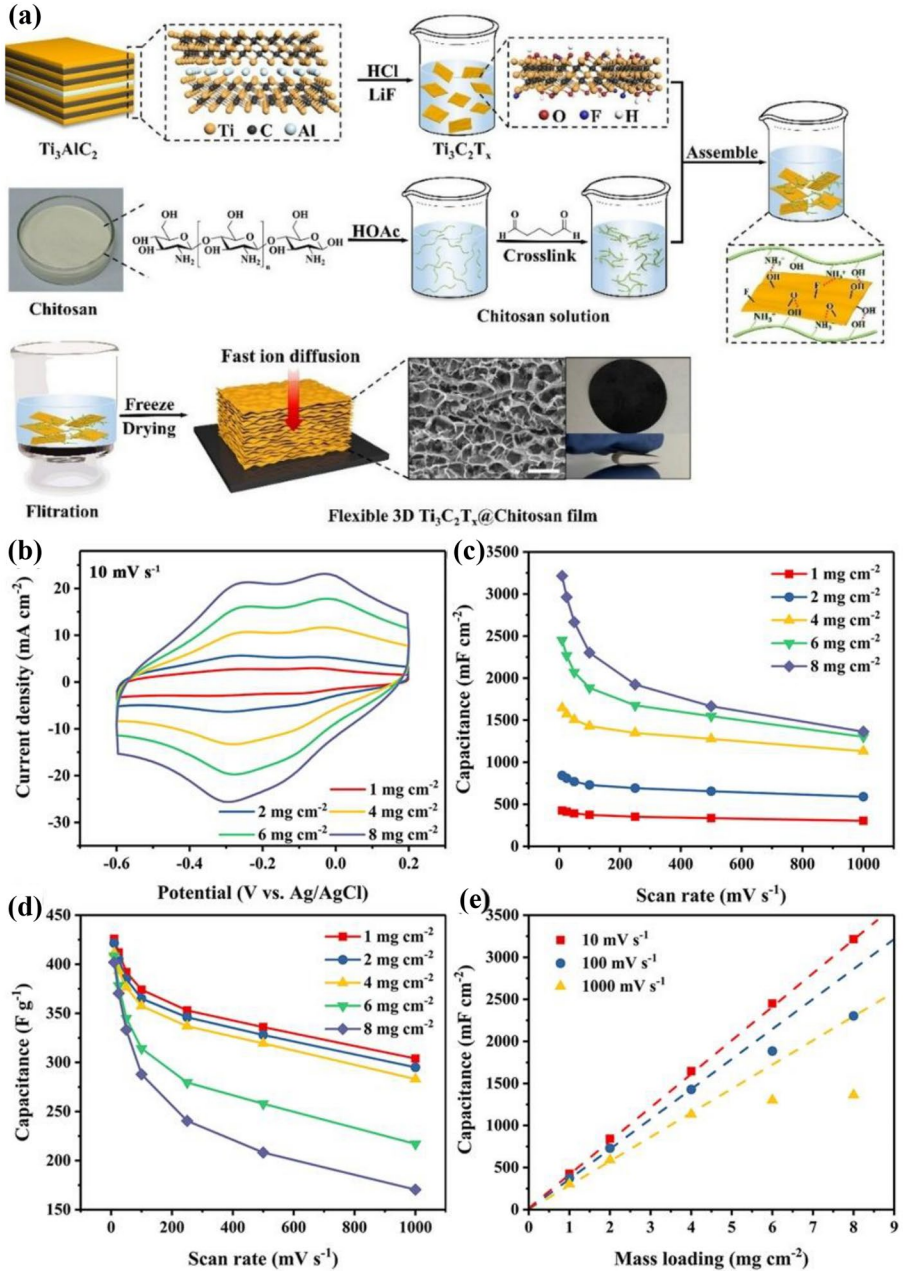

Fig. 15 (a) A schematic representation of the fabrication of flexible $Ti_3C_2T_x$ MX/CS film: and $Ti_3C_2T_x$ MX/CS electrodes electrochemical performance in a 3M H_2SO_4 electrolyte with mass loading ranging from 1 to 8 mg/cm^2. (b) CV curves at 10 mV/s scan rate. At scan speeds ranging from 10 to 1000 mV/s., (c) areal capacitance and (d) gravimetric capacitance were measured. (e) A linear connection between the electrode mass loadings and the areal capacitance was obtained. Reproduced with permission [214] Copyright 2022, Elsevier B.V

volume variations during lithium intercalation and enhancing electrical conductivity, CS serves as a binder to improve silicon anodes, achieving discharge capacities of 942.4 mAh/g after 50 cycles [232, 233].

A study by X. Li et. al. of silicon/CS/MX (SCM) composites (see Fig. 16), in which CS functions as a charge bridge and forms a hierarchical conductive network that reduces silicon volume expansion and enhances the anode performance of lithium-ion batteries. In the meantime, during the composite fabrication process, CS functions as a charge

Table 6 Highlighted studies of MX/CS composites and their use in supercapacitor

Electrode	Capacitance	Current density	Power/Energy density	Capacitance retention	References
MX/CS	245.2 F/g	0.2 Vs^{-1}	143.2 mWh/cm^2 Power Density	57.1% (400 folds)	[214]
MX/CS/BM	1801.4 mF/m^3	2 mVs^{-1}	33.4 Wh/L Energy Density	82% (50,000 cycles)	[215]
MX/CS-PCM	362 F/g	0.5 A/g	27.8 W/kg (ED) 500 W/kg (PD)	93.87% (10,000 cycles)	[216]
MX/CS	286.28 F/g	3 A/g	21.47 Wh/kg (ED) 2343.75 W/kg (PD)	98% (10,000 cycles)	[217]
MX/CS	309 F/g	1 A/g	20 Wh/kg (ED) 581 W/kg (PD)	92.4% (10,000 cycles)	[218]
MX/CS/PAA/CoS	3.6 F/g	4 mA/g	~	80% (2,000 cycles)	[219]
MX/CS/PAA/PbS	77.05 F/g	10 mA/g	~	89% (2,000 cycles)	[220]
MX/CS/PAA	291.8 mF/g	0.5 mA/g	0.023 Wh/kg (ED) 5.43 W/kg (PD)	64.24% (2,000 cycles)	[221]
MX/CS	1083 F/cm^3	5 mV/s	77.6 mWh/ cm^3 (ED) 3,617.7 mW/cm^3 (PD)	98.1% (10,000 cycles)	[71]

BM: Biomass, CS-PCM: Chitosan derived porous carbon microsphere, PAA: Polyacrylic acid

bridge, sequentially interacting with the silicon and MX nanosheets under electrostatic force. The N-doped carbon layer and MX nanosheet that accumulate during CS calcination are responsible for creating a hierarchical, high-speed conductive network over the silicon surface, which helps to reduce the volume growth of silicon. With a capacity retention of 76.2%, the SCM electrode achieved a constant discharge capacity of 900.8 mAh/g at 0.5 A/g, 861.9 mA/g at 1 A/g, and 657.6 mA/g even at 2 A/g after 100 cycles. The SCM electrodes have an initial coulombic efficacy (ICE) of 81.5% and initial discharge/charge capacities of 2082.5/1698.1 mAh/g. For SCM electrodes, the second and third cycle CEs are 95.3% and 96.7%, respectively. Following five cycles under 0.2, 0.5, 1.0, 2.0, and 5.0 A/g, respectively, the specific capacity of the SCM electrode is 1848.8, 1429.6, 1008.3, 626.9, and 216.0 mAh/g. The charge-transfer resistance (Rct) of SCM [234]. The enormous potential of the MX/CS composite can be understood by taking a look at Table 7, where we highlighted some of the recent works.

4.6 Fire hazard protection

MX excels in preventing fire hazards because it can withstand high temperatures without degrading, making it a suitable option for flame-retardant coatings or structural reinforcements. Variants of MX can readily withstand temperatures between 500–800 °C, and with surface modification, they can reach up to 1000 °C [239–241]. When burning, several MXs (such as $Ti_3C_2T_x$, Ti_2CT_x, Mo_2CT_x, and V_2CT_x) facilitate the formation of a protective layer of char that insulates the underlying material and restricts the release of combustible gases. It is a viable candidate due to its exceptional tensile strength ($Ti_3C_2T_x$ nanosheets have recorded tensile strengths of up to 15.4 GPa) and mechanical strength (e.g., Young's moduli for $Ti_3C_2T_x$ range about 300–500 GPa) [242, 243]. CS is unique due to its ability to assist with the release of non-flammable gases, improve thermal stability, and promote the production of char during combustion. CS is a nitrogen-rich biopolymer that suppresses smoke and dilutes combustible gases; it also emits water vapor and gases, including nitrogen, when it burns. Due to these qualities,

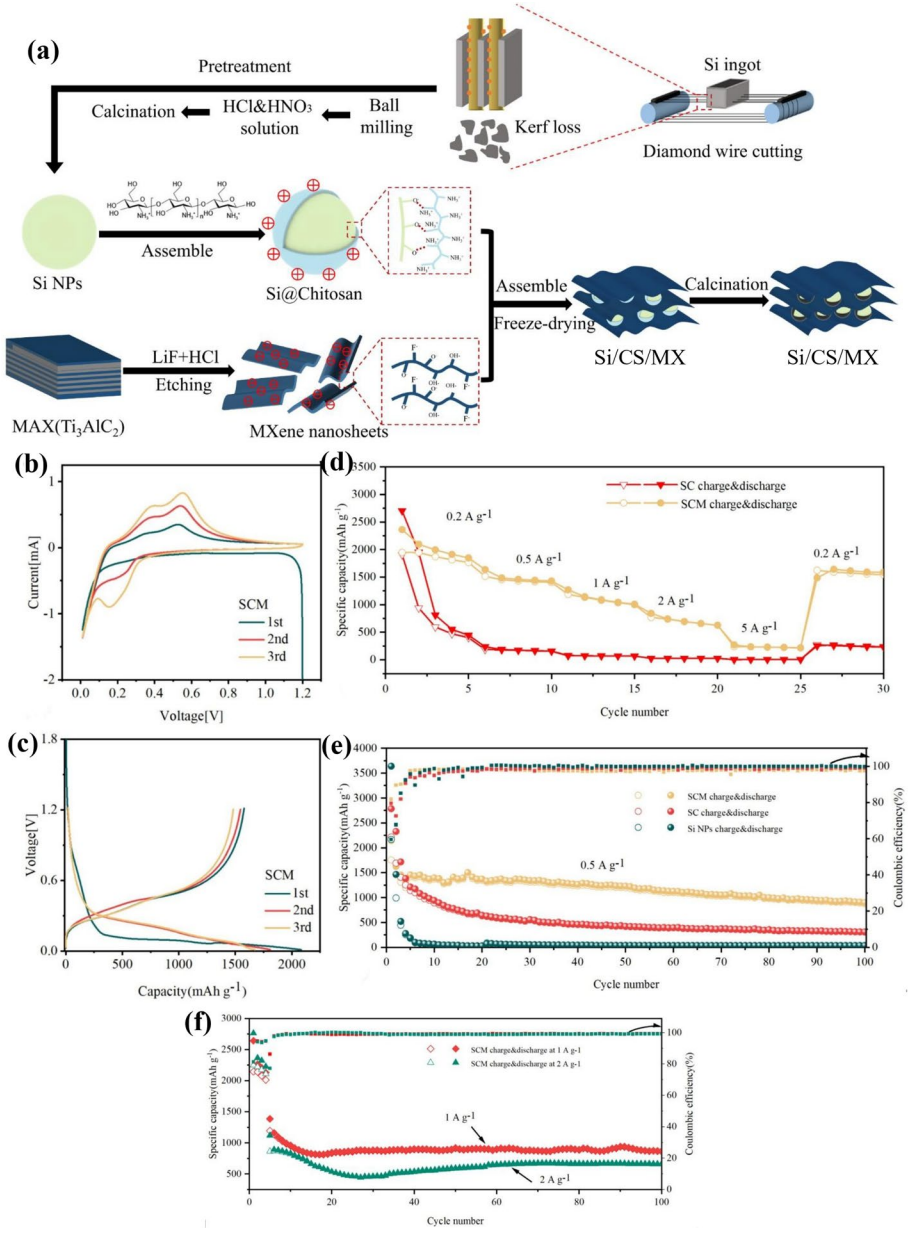

Fig. 16 (a) Illustration of the synthesis process of silicon/CS/MX (SCM) composite: (b) SCM electrode CV curves for the first 3-cycles. (c) SCM electrode GCD curves for the first 3-cycles at 0.1 A/g. (d) SC and SCM electrode rate capability. (e) Si NPs, SC, and SCM electrode cycle performance at 0.5 A/g. (f) SCM electrode cycle performance at 1 and 2 A/g. Reproduced with permission [234] Copyright 2024, Elsevier B.V

CS is a desirable alternative to artificial flame retardants, which can contain hazardous chemicals. Moreover, CS can be readily incorporated into fabrics, foams, and coatings to enhance fire resistance due to its ability to form films [244–246].

Employing a straightforward chemical modification technique, L. Liu et al. successfully created a unique hybrid of modified MX with phosphorylated CS (PC) to produce cotton fabric (CF) textiles with high-efficiency flame retardancy. It was later used in the impregnation procedure to create PC/T-MX-functionalized cotton fabric (PC/T-MX/CF) (see Fig. 17). Pure cotton, PC/T-MX/CF1, PC/T-MX/CF2, PC/T-MX/CF3, and PC-CF were the five samples that were created. The thermal and flame-retardant performance of

Table 7 Highlighted studies of MX/CS and MX/CS hybrid composites and their application in batteries

Electrode	Battery type	Capacitance	Current density	Capacitance retention	References
Si/CS/MX	Lithium-ion battery	2082.5 mAh/g	0.1 A/g	61.8% (100 cycles)	[234]
MX/NOC-CS/Se	Lithium-Selenium battery	866 mAh/g	0.1 A/g	97.3% (100 cycles)	[235]
MX/CS/Zn	Zinc-ion battery	166 mAh/g	0.5 A/g	76% (400 cycles)	[228]
MX/CS/TiO_2	Lithium-Sulfur battery	1439 mAh/g	0.1 C	61.6% (200 cycles)	[236]
MX/CS/Zn	Aqueous Zinc-based batteries	409 mAh/g	0.5 A/g	~100% (CE) (42,000 cycles)	[237]
MX/CS/Tungsten	Lithium-ion battery	223 mAh/g	0.042 mA	~99.99% (2,000 cycles)	[238]
MX/CS/Tungsten	Sodium-ion battery	210.8 mAh/g	0.042 mA	~99.99% (2,000 cycles)	[238]

NOC-CS: Nitrogen & Oxygen doped porous carbon derived from chitosan, Zn: Zinc, CE: Coulombic efficiency

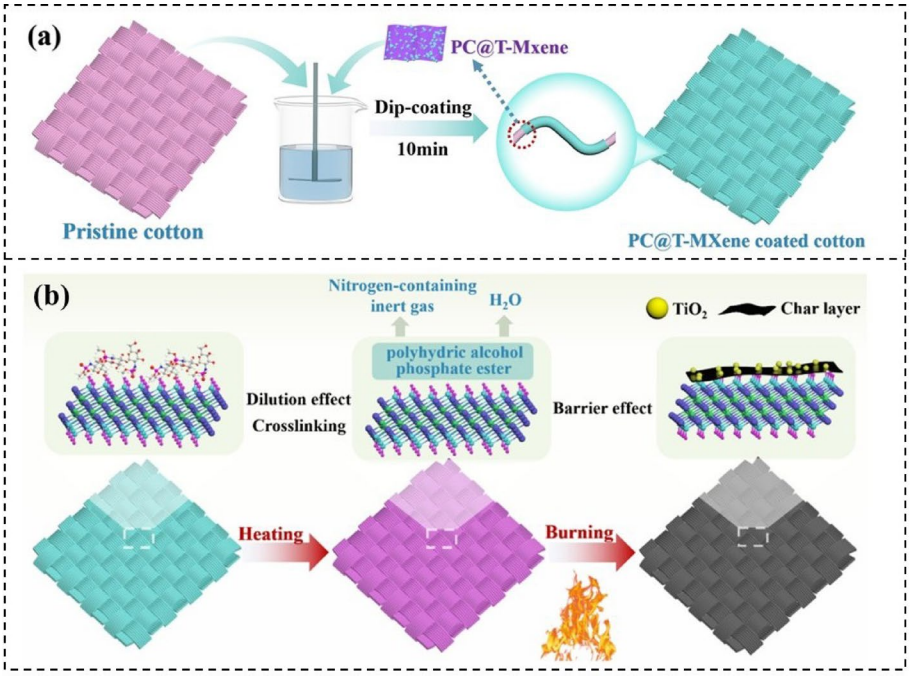

Fig. 17 (a) A schematic representation of how cotton textiles coated with PC/T-MX/CF are fabricated. (b) A schematic representation of the potential flame-retardant mechanism for PC/T-MX/CF. Reproduced with permission [247] Copyright 2025, Elsevier B.V

PC/T-MX/CF3 was noticeably better than that of the original cotton textile and the PC-decorated cotton fabric (PC-CF). In the TGA investigation, PC/T-MX/CF3 maintained 39.1% of the char residue at high temperatures in a nitrogen environment, with the treated cotton fabric's weight increasing by 12%. The LOI of PC/T-MX/CF3 increased considerably to 35% (compared to 20% for pure cotton), satisfying the flame-retardant requirements. In contrast to complete combustion of pure cotton, PC/T-MX/CF3 self-extinguished with a char length of 57 mm, according to the vertical burning test (VBT). Compared to pure cotton (212.3 kW/m^2), PC/T-MX/CF_3 exhibited an 80.7% reduction

in peak heat release rate (PHRR), achieving a value of 41.0 kW/m^2. When compared to the original cotton textile, the total heat release (THR) decreased by 43.7% (from 12.6 MJ/m^2 to 7.1 MJ/m^2). Additionally, after three washings, PC/T-MX/CF3 maintained its self-extinguishing qualities and flame retardancy, with only a 15.7% mass loss [247]. Some of the recent works involving MX/CS composite in fire hazard protection are highlighted in Table 8, which may provide a better insight into the effectiveness of the composite in this particular application.

4.7 Solar evaporation/Desalination

The technique of solar evaporation, also known as desalination, uses solar energy to evaporate water, filtering it of contaminants and salts before condensing the vapor to create fresh, drinkable water [259]. A potential material for solar evaporation and desalination is MX. Its photothermal qualities, which absorb sunlight across a wide range (~90% in the UV–Vis-NIR spectrum) and transform it into heat with near-100% efficiency, are what make it successful in solar desalination, according to research. Flexible MX-based textiles have been shown to have evaporation rates of 1.81 kg/m^2h and efficiencies of over 85% under a single sun. Additionally, MX has remarkable stability in saline water, preventing corrosion and biofouling [260–262]. CS is frequently used into aerogels or membranes in solar desalination to improve water movement and evaporation efficiency. Under one sun, it achieves evaporation rates of 1.55 kg/m^2h and efficiencies of 97.15%. Research also shows that it can lower the energy needed for evaporation; hydrogels that combine chitosan and poly (vinyl alcohol) has been shown to achieve desalination rates of 3.6 kg/m^2h, which is more than double the usual values [263–265]. Table 9 provides highlights of some of the recent works of the MX/CS composite for solar evaporation, which may provide additional understanding about the potential of the composite in this sector.

A polyurethane/CS/MX (APCM) aerogel with a directed channel structure was first created as a solar evaporator for desalination using the freeze-casting technique, according to research by M. Sun et al. To compare the results of the experiment, a homogenous mixture of PU/CS/MX (PCM) was also poured into a polydimethylsiloxane mold. Under 1-sun irradiation, a reasonable evaporation rate (1.81 kg/m^2h) and excellent evaporation efficiency (85.07%) were attained. Using waterborne polyurethane (PU) and CS as matrix materials provided the evaporator with favorable mechanical stability, enabling it to float steadily on high-concentration salt water for more than 2 weeks and continuously achieve a high evaporation rate for 12 hours under 1-sun irradiation. Rapid water/ion flow was made possible by the wood-inspired anisotropic structure with 88.19% porosity, as revealed by scanning electron microscope (SEM) images. Because of its aligned channels, which are essential for salt resistance, APCM absorbed water 33 times quicker than disordered PCM. APCM exhibits exceptional light absorption capabilities, with an average absorption of 96% over the UV–Vis-NIR (200–2500 nm) spectrum. The surface temperature increased to 83.9 °C during 1-sun irradiation (compared to 31.6 °C for the MX-free APC) and reached 138 °C under 5-sun irradiation, demonstrating that the low thermal conductivity (0.298 W/mK) reduced heat loss and increased efficiency. A photothermal conversion efficiency of 85.07% is ultimately achieved under 1-sun conditions. Under three sun density conditions, the evaporation efficiency was 91.3%. In simulated saltwater, even the concentrations of the four target metal ions (Na^+, Mg^{2+}, Ca^{2+}, and K^{2+}

Table 8 Highlighted examples of MX/CS composites and their application for the prevention of fire/fire-related hazards

Composite/Matrix	Structure	Effectiveness/Performance	References
MX/CTNC	Film based Fire Alarm	Trigger Time: 0.78 s	[248]
		Response Time: 290 s	
		Thermal stability: up-to 800 °C	
MX/UCS/APP	Bamboo-based fire alarm device	Trigger Time: 2 s	[249]
		Thermal stability: uo-to 500 °C	
		Self-healing: 178 s under NIR	
MX/CS/GO	Aerogel based fire alarm device	Trigger Time: 9.65 s	[250]
		Response Time: 120.40 s	
MX/CTNC/APP	Film based Fire alarm device	Trigger Time: 1 s	[251]
		Response Time: 120 s	
MX/CS	Coating on Cotton Fabric (CF)	PHRR: reduced by 80.7% compared to pure cotton fabric	[247]
		THRR: reduced by 43.7% compared to pure cotton fabric	
		Thermal Stability: 800 °C	
		LOI: 35%	
		Self-extinguishing: < 1 s	
Q-MX/PCS/SPI	Coating on Plywood board	PHRR: reduced by 71.5% compared to Pristine SPI	[252]
		THRR: reduced by 32.8% compared to Pristine SPI	
		Self-extinguishing: < 1 s	
		Residual mass: increased by 6.15% than Pristine SPI	
MX/PCS/PA	Coating on Polyurethane foam (PUF)	PHRR: reduced by 51.1% compared to pure PUF	[253]
		THRR: reduced by 84.8% compared to pure PUF	
		Thermal Stability: 700 °C	
		COPR: reduced by 60.4%	
		CO_2PR: reduced by 69.1%	
MX/CMC	Coating on Cotton Fabric for multi-functional purposes	Trigger time: 10 s	[254]
		PHRR: reduced by 66% compared to pure cotton fabric	
		Thermal Stability: 400 °C	
		LOI: 45.5%	
		Char length: 33 mm	
MX/CS/PCNF	Film based Flame-retardant material	PHRR: reduced by 25.6% compared to pure PCNF	[255]
		THRR: reduced by 20.9% compared to pure PCNF	
		Char Residue: increased by 39.1% compared to pure PCNF	
		Thermal Stability: 800 °C	
MX/CS	Coating on Polyurethane foam (PUF)	PHRR: reduced by 57.2% compared to pure PUF	[256]
		THRR: reduced by 65.5% compared to pure PUF	
		TSR: reduced by 71.1% compared to pure PUF	
		COPR: reduced by 70.8%	
		CO_2PR: reduced by 68.6%	
MX/CS	Coating on Polyurethane foam (PUF)	PHRR: reduced by 66.3% compared to pure PUF	[257]
		PSPR: reduced by 51.6% compared to pure PUF	

Table 8 (continued)

Composite/Matrix	Structure	Effectiveness/Performance	References
		TSR: reduced by 65.5% compared to pure PUF	
		Thermal stability: 750 K	
MX/PCS	Coating on Thermoplastic polyurethane (TPU)	PHRR: reduced by 66.7% compared to pristine TPU	[258]
		THRR: reduced by 21.0% compared to pristine TPU	
		TSR: reduced by 27.7% compared to pristine TPU	

PHRR: Peak Heat Release Rate, THRR: Total Heat Release Rate, COPR: CO Production Rate, CO_2PR: CO Production Rate, LOI: Limiting Oxygen Index, TSR: Total smoke release, PSPR: Peak Specific Peak Rate, Q-MX: Quaternary ammonium-functionalized MXene, CTNC: Chitin Nanocrystal, CMC: Carboxymethyl Chitosan, PCS: Phosphorylated chitosan, PA: Phytic Acid, PCNF: Phosphorylated cellulose nanofibril, UCS: UPy-NCO treated Chitosan, APP: Ammonium Polyphosphate, GO: Graphene Oxide, TPU: Thermoplastic polyurethane, SPI: Soybean protein isolate based adhesives

Table 9 A highlighted example of MX/CS composites and their use for solar evaporation/desalination

System	Structure	Evaporation Rate (kg/m^{2}h)	Evaporation efficiency (%)	Evaporation Factor	References
MX/CS/PU	Aerogel	1.81	85.07	absorbed 96% sunlight	[266]
MX/CS/LG	Aerogel	2.351	88.22	absorbed 95.50% sunlight	[267]
MX/CS	Aerogel	1.80	75.20	absorbed > 90% sunlight	[268]
MX/CS/rGO/PDA	Aerogel	1.86	83.28	absorbed ~ 95% sunlight	[269]
MX/CS/KF	Aerogel	4.40	94.8	absorbed 92.7% sunlight	[60]
MX/CS	Aerogel	2.44	92.2	absorbed > 96.2% sunlight	[61]
MX/CS/CdS/PVA	Hydrogel	1.63	~ 75	absorbed 90% sunlight	[270]
Ag-MX/CS	Hydrogel	1.59	93	Sunlight intensity 1 kW/m^2	[271]
Ag-MX/CS	Hydrogel	3.22	94.9%	Sunlight intensity 0.2 W/cm^2	[272]
MX/CSM/GA	2 Layer DISVG	2.63	99	Sunlight intensity 1 kW/m^2	[58]
MX/CS/PF	Fabric composite	1.50	88.05	Sunlight intensity 1 kW/m^2	[205]
MX/CS/LSC/PVA	Hydrogel	2.75	92.30	absorbed ~ 95.5% sunlight	[273]
MX/CS/MF	3D Composite	1.428	89.80	Sunlight intensity 1 kW/m^2	[274]
MX/CS	Aerogel	3.99	90	Sunlight intensity 3 kW/m ^{2}	[275]
MX/CS/MoS_2/GA/CF	Janus composite	2.29	93.8	Sunlight intensity 1 kW/m^2	[276]

CSM: Chitosan Monolith, MX: MXene, PU: Polyurethane, LG: Lignin, MF: Melamine foam, PVA: Polyvinyl alcohol, rGO: Reduced Graphene Oxide, PDA: Polydopamine, LSC: $La_{0.5}Sr_{0.5}CoO_3$, Ag: Silver, PF: Polymer fabric, DISVG: Degradable interfacial solar vapor generator, GA: Glutaraldehyde, CF: Carbon Fiber, KF: Kapok fiber

) dropped by three to four orders of magnitude [266]. The formation steps of the APCM and the performance of the APCM system are represented in Fig. 18.

4.8 Solvent dehydration

The process of extracting water from a solvent to produce a dry or anhydrous state is known as solvent dehydration. A variety of processes, including distillation, the use of drying agents (such as molecular sieves), or sophisticated technologies like membrane-based pervaporation or vapor permeation, can be used to dehydrate a solvent [277].

Depending on the composition (e.g., $Ti_3C_2T_x$), the surface terminations of MXs (e.g., -OH, -O) provide water adsorption capabilities of up to 0.5–1 g of water per gram of MX. For ethanol–water combinations (e.g., 90% ethanol, and 10% water), the separation factors (water/solvent selectivity) of the MX-based membrane exceed 1,000. Significant

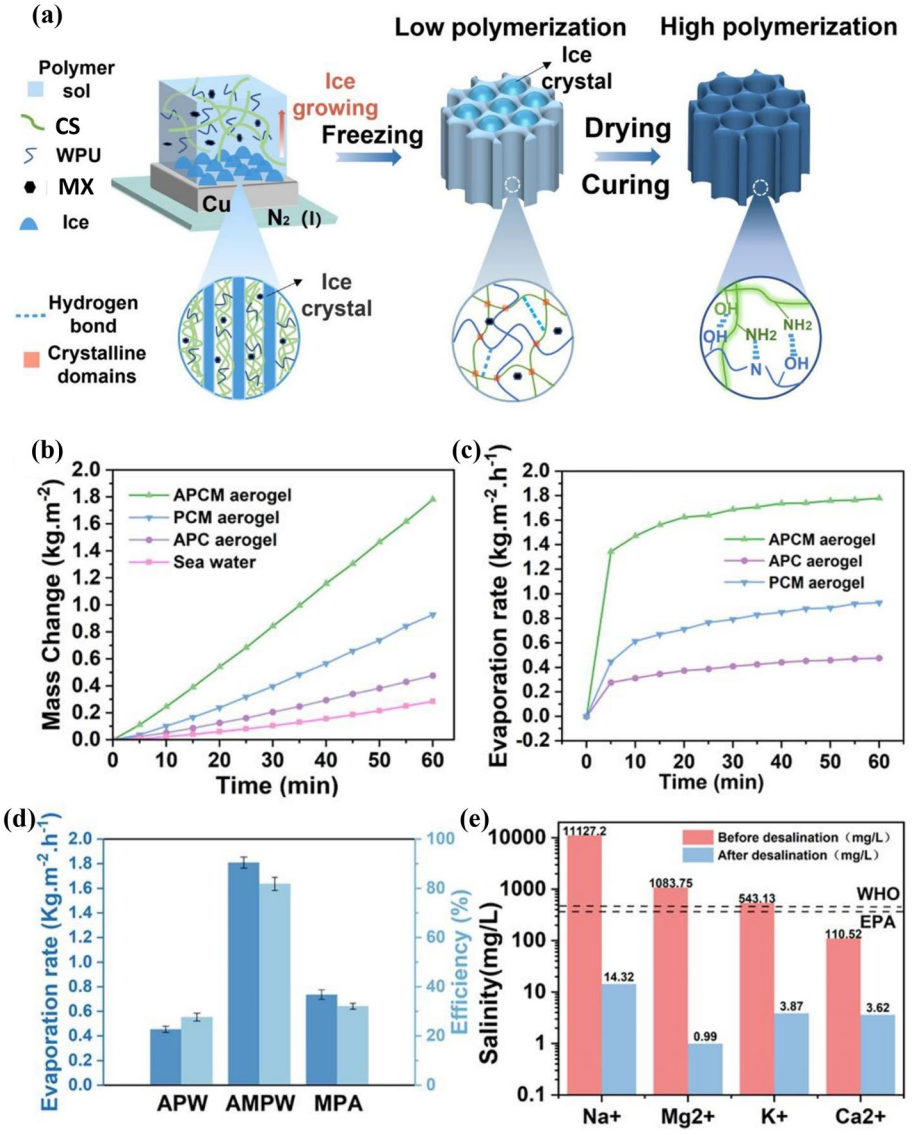

Fig. 18 (a) An illustration of the manufacturing process of the APCM solar evaporation system and performance. (b) Variation in the evaporation mass of APCM, PCM, and APC under one-sun irradiation. (c) Evaporation rate of APCM, PCM, and APC under one-sun irradiation. (d) The efficiency of APCM, PCM, and APC evaporation when exposed to a single sun. (e) Major metal ion concentrations in seawater simulations both before and after desalination. Reproduced with permission [266] Copyright 2023, Elsevier B.V

variables include high surface areas (100–500 m^2/g) and flow rates (1–2 kg/m^2h). Compared to pure polymer membranes, MXenes increase water permeability by 50–200% when added to polymer matrices [8, 278, 279]. The hydroxyl and amino groups of chitosan provide it with water sorption capabilities of 0.3–0.6 g/g, which enables membranes to extract water from solvents like ethanol in a selective manner (e.g., lowering water from 10% to < 0.5%). Crosslinked CS membranes pervaporate 90% ethanol–water mixtures at 60 °C with water flow rates of 0.5–1.5 kg/m^2h and separation factors of 500–2,000. One CS-PVA mix membrane, for example, demonstrated a separation factor of 1,800 and a flux of 1.2 kg/m^2h. Furthermore, in continuous dehydration processes, CS extends operating lifespans from weeks to months by reducing biofouling by 70–90% compared to synthetic membranes [280–282].

Z. Xu et al. created a novel MX/CS mixed matrix membrane for solvent dehydration via a pervaporation technique by combining $Ti_3C_2T_x$ MX nanosheets with CS. The MX/CS MMMs, also known as the spin-coating manufacturing process, were created by physically combining the MX nanosheets that were dispersed in water with the CS solution. The membrane dehydration performance was assessed using three different types of organic solvents: ethanol, ethyl acetate, and dimethyl carbonate. With total fluxes of around 1.4 to 1.5 kg/m^2h and separation factors of 1421, 4898, and 906, respectively, the 3% weight MX/CS MMM showed exceptional efficacy for dehydrating ethanol, ethyl acetate, and dimethyl carbonate. Additionally, a total flow of 1428 g/m^2h was attained during the experiment. The investigation demonstrated that filler aggregation caused by higher MX loading (5 weight percent) resulted in decreased performance. The standard feed temperature and pressure for the experiment were 323 K and 200 Pa, respectively. However, it also demonstrated that raising the feed temperature enhanced flow while decreasing the separation factor because of polymer matrix swelling. The weight percentage of feed water was 2%. Good long-term stability was indicated by the membrane's steady performance for 1800 min of continuous operation. Pervaporation performance for solvent dehydration was significantly improved by the addition of MX nanosheets to CS membranes, with the best outcomes achieved at a 3% MX loading. The study emphasizes how MX-based membranes might be used in industrial separation procedures [283].

5 Challenges and future aspects

Since the MX/CS composite has garnered considerable research interest, it presents several issues and opportunities for improvement. The most evident difficulty is the synthesis of MX. The costly and risky synthesis method, which frequently employs hazardous chemicals such as HF, limits industrial scalability. The synthesis of CS is a remarkable challenge. The process is highly sophisticated, and even a small calculation error or mistake can result in the massive loss of chemicals and raw materials [55, 192, 284].

Large-scale commercial manufacturing of MXs is hampered by the high price and low yield of current fabrication techniques. Due to a lack of scalable, affordable, and repeatable industrial techniques, MX synthesis is still mostly done in laboratories. Top-down techniques, like HF etching, complicate scaling and provide health and environmental hazards. Optoelectronic properties are hampered by the MXs produced by current processes, which have uneven layer thicknesses, stacking, and vacancies. Additionally, the repulsive interactions between negatively charged MX nanosheets make it difficult to precisely manage in-plane pores and interlayer spacing (d-spacing), which results in uneven nanoslits and decreased selectivity. High MX mass loading decreases porosity (from 59 to 39%), increasing tortuosity and decreasing permeability, and repulsive forces upset orderly layer stacking [136, 285–288].

Aggregation and restacking of MX nanosheets is a significant problem since it lowers their active surface area and can impair their effectiveness in energy storage and adsorption applications. MX membranes have a propensity to expand in water-based solutions, which affects their long-term durability and efficacy, especially in water treatment applications. Van der waals forces lead to the aggregation of nanosheets, which decreases the available surface area and conductivity of MX. The mechanical weakness of MX, such as its brittleness, restricts the integration of flexible devices, including wearable sensors.

Use in high-power devices is limited by performance degradation at high temperatures (> 150 °C). The majority of research is on Ti_3C_2. Despite their potential, other MXs (such as V_4C_3 and Mo_2TiC_2) are still not well understood [287, 289–292].

Over time, the stability and performance of MXs may be impacted by their susceptibility to oxidation. MXs shorten shelf life and device lifespan by degrading quickly in ambient/oxygen-rich settings (e.g., $Ti_3C_2T_x$ conductivity reduces by 50% after 24 hours in air). To prevent oxidation, polymers can be encapsulated (e.g., PVA, polydopamine) or their terminal groups modified (O/OH rather than F). Before widespread real-world applications can be achieved, a more comprehensive assessment of the long-term toxicity, degradability, biosafety, cytotoxicity, and biocompatibility of MXs is necessary. To comprehend and lessen the possible harmful consequences and environmental implications of MX-based compounds, thorough life cycle assessments are required. Aquatic toxicity is shown by preliminary evidence (e.g., Ti_3C_2 ecotoxicity > 1 L/mg). Impacts on the life cycle are not evaluated [287, 293–296].

Despite all of those worries, there is still opportunity for advancement, such as the use of machine learning to forecast the best synthesis parameters and bandgaps and the use of alkali/molten salt techniques (such as NaOH/LiF) to replace HF. combining MXs with nanomaterials (like graphene) or polymers (like PEDOT:PSS) to increase their conductivity and mechanical strength. Another potential area of development is tuning by surface termination to engineer the bandgap for photodetectors/LEDs. In order to get from lab-scale prototypes to practical applications in wearables, AI-driven imaging, and sustainable electronics, future success depends on multidisciplinary initiatives that combine computational screening, improved manufacturing, and system-level engineering [287, 297–299].

6 Conclusions

Through the combination of biocompatibility, processability, and adsorption capacity, CS with the unmatched electrical conductivity, photothermal efficiency, and surface reactivity of MXs, these composites surpass the constraints of their constituent parts. Their customizable designs and functional group interactions enable their exceptional versatility in EMI shielding, sensing, energy storage, and environmental remediation applications. The vulnerability of MX to oxidative degradation, the incompatibility between the hydrophilic CS and MX layers at the interface, and the limitations of scalability in composite production remain significant obstacles. Advanced interfacial engineering, advancements in covalent functionalization, and scalable synthesis methods, such as extrusion or roll-to-roll processes, are needed to overcome these obstacles. To further accord with the concepts of the circular economy, their growth must be supported by sustainable practices, such as the use of bio-derived chitosan and environmentally friendly MX synthesis pathways. MX/CS composites have enormous potential to be considered as the top priority to move toward green technology and multipurpose materials. Future design and developments, thorough lifecycle analyses, and industry collaborations will be crucial in transforming these materials from laboratory discoveries into practical applications. MX/CS composites are positioned to revolutionize next-generation applications by striking a balance between sustainability and performance, thereby bridging the gap between ecological responsibility and high-tech innovation.

Acknowledgements
The authors would like to acknowledge Gopalganj Science and Technology University, Gopalganj-8100, Bangladesh, for their kind support.

Author contributions
Conceptualization: S.A.H., M.H.M., M.K., and T.I.; Data Curation: S.A.H., and M.H.M.; Investigation: M.N.; Methodology: M.R.R., and T.I.; Supervision: M.K., and T.I.; Project Administration: M.K., and T.I.; Writing – Original Draft Preparation: S.A.H., M.H.M.; Writing – Review & Editing: S.A.H., M.H.M., M.K., M.N., M.R.R., and T.I. All authors read, and approved the final revised manuscript.

Funding
Not applicable.

Data availability
In this review, no new data were generated or analyzed during this work. All information presented is derived from previously published sources, which are appropriately cited throughout the manuscript.

Declarations

Ethics consent to participate
Not applicable.

Consent to publish
Not applicable.

Competing interests
The authors declare no competing interests.

Author details
[1]Department of Applied Chemistry and Chemical Engineering, Faculty of Engineering, Gopalganj Science and Technology University, Gopalganj 8100, Bangladesh
[2]Department of Textile Engineering, Uttara University, Dhaka 1230, Bangladesh
[3]Department of Chemistry, Faculty of Science, Gopalganj Science and Technology University, Gopalganj 8100, Bangladesh
[4]Department of Industrial and Production Engineering, Bangladesh University of Textiles, Dhaka 1208, Bangladesh
[5]Department of Textiles, Merchandising, and Interiors, University of Georgia, Athens, GA 30602, USA
[6]Department of Textile Engineering, Jashore University of Science and Technology, Jashore 7408, Bangladesh

Received: 20 May 2025 / Accepted: 3 September 2025
Published online: 16 December 2025

References

1. Rana AK, Gupta VK, Hart P, Scarpa F, Thakur VK. Sustainable MXene-chitosan/chitin composites for interdisciplinary applications in water purification, bio-medical, bio-sensing and electronic fields. Mater Today Sustain. 2024;25:100671.
2. Riazi H, Taghizadeh G, Soroush M. MXene-based nanocomposite sensors. ACS Omega. 2021;6:11103–12.
3. Chang L, et al. Review—Ti3C2Tx MXene: an emerging two-dimensional layered material in water treatment. ECS J Solid State Sci Technol. 2021;10:047002.
4. Chen Y, et al. MXene-based electrodes for supercapacitor energy storage. Energy Fuels. 2022;36:2390–406.
5. Xiao Z, Li Z, Meng X, Wang R. MXene-engineered lithium–sulfur batteries. J Mater Chem A. 2019;7:22730–43.
6. Han M, et al. Beyond Ti3C2Tx: MXenes for electromagnetic interference shielding. ACS Nano. 2020;14:5008–16.
7. Che X, et al. Mildly peeling off and encapsulating large MXene nanosheets with rigid biologic fibrils for synchronization of solar evaporation and energy harvest. ACS Nano. 2022;16:8881–90.
8. Wu Y, Ding L, Lu Z, Deng J, Wei Y. Two-dimensional MXene membrane for ethanol dehydration. J Memb Sci. 2019;590:117300.
9. Ma L, Wang Y, Gao J, Zhu Z. Construction of MXene-based flame retardant with multiple carbonization towards for reducing fire hazard and smoke release of epoxy resin. Eur Polym J. 2024;215:113253.
10. Zhang N, et al. MOF/MXene-loaded PVA/chitosan hydrogel with antimicrobial effect and wound healing promotion under electrical stimulation and improved mechanical properties. Int J Biol Macromol. 2024;264:130625.
11. Li Y, et al. Remarkable enhancement of corrosion resistance and tribological properties of chitosan-MXene based hydrogel coating on the surface of Ti6Al4V alloy. Tribol Int. 2024;192:109229.
12. Siva Sangu S, Chandra Bose Gopinath S, Abdul Shukur MF, Mohamed Saheed MS. An electrochemical approach for ultrasensitive detection of zearalenone in commodity using disposable screen-printed electrode coated with MXene/chitosan film. Bionanoscience. 2022;12:814–23.
13. Saha R, Munshi MH, Akter M, Shikder AAR, Islam T. Synthesis techniques, fundamental properties, and emerging applications of nanocomposites: a comprehensive review. SPE Polym. 2025. https://doi.org/10.1002/pls2.70004.
14. Cao WT, et al. Binary strengthening and toughening of MXene/cellulose nanofiber composite paper with nacre-inspired structure and superior electromagnetic interference shielding properties. ACS Nano. 2018;12:4583–93.
15. Wang L, Wang DP, Wang K, Jiang K, Shen G. Biocompatible MXene/chitosan-based flexible bimodal devices for real-time pulse and respiratory rate monitoring. ACS Mater Lett. 2021;3:921–9.
16. Dong Y, Sang D, He C, Sheng X, Lei L. Mxene/alginate composites for lead and copper ion removal from aqueous solutions. RSC Adv. 2019;9:29015–22.

17. Guo Z, Wang M, Qiao L, Wang J, He Z. Photothermal, magnetic, and superhydrophobic PU sponge decorated with a Fe3O4/MXene/lignin composite for efficient oil/water separation. Langmuir. 2023;39:16935–53.
18. Liang J, et al. Enhanced mechanical and electrical properties of starch-based hydrogels incorporating polyacrylic acid and MXene for advanced wearable sensors in sign language recognition. Sens Diagn. 2024;3:256–68.
19. Yang W, et al. Multifunctional MXene/natural rubber composite films with exceptional flexibility and durability. Compos B Eng. 2020;188:107875.
20. Iravani P, Iravani S, Varma RS. MXene-chitosan composites and their biomedical potentials. Micromachines. 2022;13:1383.
21. He X, et al. A high-performance waterborne polymeric composite coating with long-term anti-corrosive property based on phosphorylation of chitosan-functionalized Ti3C2Tx MXene. Adv Compos Hybrid Mater. 2022;5:1699–711.
22. Mayerberger EA, Street RM, McDaniel RM, Barsoum MW, Schauer CL. Antibacterial properties of electrospun Ti 3 C 2 T z (MXene)/chitosan nanofibers. RSC Adv. 2018;8:35386–94.
23. Ghanbari R, Nazarzadeh Zare E. Engineered MXene-polymer composites for water remediation: promises, challenges and future perspective. Coord Chem Rev. 2024;518:216089.
24. Malaki M, Varma RS. Mechanotribological aspects of MXene-reinforced nanocomposites. Adv Mater. 2020;32:2003154.
25. Zha XH, et al. The thermal and electrical properties of the promising semiconductor MXene Hf2CO2. Sci Rep. 2016;6:1–10.
26. Hantanasirisakul K, et al. Effects of synthesis and processing on optoelectronic properties of titanium carbonitride MXene. Chem Mater. 2019;31:2941–51.
27. Shukla V. The tunable electric and magnetic properties of 2D MXenes and their potential applications. Mater Adv. 2020;1:3104–21.
28. Hussain I, et al. Flexible MXenes for printing energy storage devices. Chem Eng J. 2024;497:154978.
29. Sahoo S, et al. Non-Ti MXene: an emerging class of 2D materials for non-Li batteries. Carbon. 2024;229:119537.
30. Sahoo S, Kumar R, Hussain I, Zhang K. Heteroatom doping in 2D MXenes for energy storage/conversion applications. Adv Powder Mater. 2024;3:100246.
31. Shuck CE, et al. Effect of Ti3AlC2 MAX phase on structure and properties of resultant Ti3C2Tx MXene. ACS Appl Nano Mater. 2019;2:3368–76.
32. Lim GP, et al. Synthesis, characterization and antifungal property of Ti3C2Tx MXene nanosheets. Ceram Int. 2020;46:20306–12.
33. Célérier S, et al. Hydration of Ti 3 C 2 T x MXene: an interstratification process with major implications on physical properties. Chem Mater. 2019;31:454–61.
34. Akgenc B. New predicted two-dimensional MXenes and their structural, electronic and lattice dynamical properties. Solid State Commun. 2019;303–304:113739.
35. Sinopoli A, Othman Z, Rasool K, Mahmoud KA. Electrocatalytic/photocatalytic properties and aqueous media applications of 2D transition metal carbides (MXenes). Curr Opin Solid State Mater Sci. 2019;23:100760.
36. Venkateshalu S, Grace AN. MXenes—a new class of 2D layered materials: synthesis, properties, applications as supercapacitor electrode and beyond. Appl Mater Today. 2020;18:100509.
37. Guo Y, Zhou X, Wang D, Xu X, Xu Q. Nanomechanical properties of Ti3C2 Mxene. Langmuir. 2019;35:14481–5.
38. Schultz T, et al. Surface termination dependent work function and electronic properties of Ti3C2Tx MXene. Chem Mater. 2019;31:6590–7.
39. Zhang Y, et al. Theoretical study on the electrical and mechanical properties of MXene multilayer structures through strain regulation. Chem Phys Lett. 2020;760:137997.
40. Maleski K, Ren CE, Zhao MQ, Anasori B, Gogotsi Y. Size-dependent physical and electrochemical properties of two-dimensional MXene flakes. ACS Appl Mater Interfaces. 2018;10:24491–8.
41. Morin-Crini N, Lichtfouse E, Torri G, Crini G. Fundamentals and Applications of Chitosan. In: Crini G, Lichtfouse E, editors. Sustainable Agriculture Reviews, vol. 35. Cham: Springer; 2019.
42. Younes I, Rinaudo M, Harding D, Sashiwa H. Chitin and chitosan preparation from marine sources. Structure, properties and applications. Mar Drugs. 2015;13:1133.
43. Islam S, Bhuiyan MAR, Islam MN. Chitin and chitosan: structure, properties and applications in biomedical engineering. J Polym Environ. 2016;25:854–66.
44. Muxika A, Etxabide A, Uranga J, Guerrero P, de la Caba K. Chitosan as a bioactive polymer: processing, properties and applications. Int J Biol Macromol. 2017;105:1358–68.
45. Moran HBT, Turley JL, Andersson M, Lavelle EC. Immunomodulatory properties of chitosan polymers. Biomaterials. 2018;184:1–9.
46. Cheba BA. Chitosan: properties, modifications and food nanobiotechnology. Procedia Manuf. 2020;46:652–8.
47. Shariatinia Z. Carboxymethyl chitosan: properties and biomedical applications. Int J Biol Macromol. 2018;120:1406–19.
48. Leceta I, Guerrero P, De La Caba K. Functional properties of chitosan-based films. Carbohydr Polym. 2013;93:339–46.
49. Hosseinnejad M, Jafari SM. Evaluation of different factors affecting antimicrobial properties of chitosan. Int J Biol Macromol. 2016;85:467–75.
50. Lizardi-Mendoza J, Argüelles Monal WM, Goycoolea Valencia FM. Chemical Characteristics and Functional Properties of Chitosan. In: Bautista-Baños S, Romanazzi G, Jiménez-Aparicio A, editors. Chitosan in the Preservation of Agricultural Commodities. Academic Press; 2016.
51. Rinaudo M. Chitin and chitosan: properties and applications. Prog Polym Sci. 2006;31:603–32.
52. Aranaz I, et al. Chitosan: an overview of its properties and applications. Polymers. 2021;13:3256.
53. Lin Q, et al. A dual regulation strategy for MXene-based composite membrane to achieve photocatalytic self-cleaning properties and multi-functional applications. Chem Eng J. 2022;443:136335.
54. Golmohammadpour M, Ayazi Z, Mohammad-Rezaei R. Fabrication of MXene/chitosan/polyurea nanocomposite decorated on a graphenized substrate for electro-enhanced solid-phase microextraction of diclofenac followed by its determination using differential pulse voltammetry. Microchim Acta. 2024;191:1–14.
55. Wang Y, Jiang B, Sun T, Wang S, Jin Y. A bio-inspired MXene/quaternary chitosan membrane with a "brick-and-mortar" structure towards high-performance photothermal conversion. J Mater Chem C Mater. 2022;10:8043–9.
56. Fang C, Liu J, Liu P, Chen W. Flexible and multifunctional papers with nacre-mimetic MXene/Chitosan nanostructures for Joule/Solar heating and motion monitoring. ACS Appl Polym Mater. 2024;6:8429–38.

57. Liu Y, et al. A conductive polyacrylamide hydrogel enabled by dispersion-enhanced MXene@chitosan assembly for highly stretchable and sensitive wearable skin. J Mater Chem B. 2021;9:8862–70.
58. Zhang T, et al. Facile fabrication of low-cost, degradable double-layer chitosan/MXene solar vapor generator for enhanced thermal localization efficiency. Chem Eng J. 2023;477:147025.
59. Rana AK, Gupta VK, Hart P, Scarpa F, Thakur VK. Sustainable MXene-chitosan/chitin composites for Interdisciplinary applications in water purification, bio-medical, bio-sensing and electronic fields. Mater Today Sustain. 2024;25:100671.
60. Su Q, et al. Natural fiber@MXene-engineered chitosan aerogels: thermodynamic-transport synergy for solar-driven hypersaline interfacial evaporation. Adv Sci. 2025. https://doi.org/10.1002/ADVS.202505944.
61. Zhou M, Zhang S, Zhang X. Double-layered chitosan aerogel/MXene film composites with asymmetric structure for absorption-dominated electromagnetic interference shielding and solar-driven interfacial evaporation. Adv Compos Hybrid Mater. 2025;8:1–15.
62. Das P, et al. MXene/0D nanocomposite architectures: design, properties and emerging applications. Mater Today Nano. 2023;24:100428.
63. Elbialy NS, Salam MA, Mohamed N. Chitosan-MXene-gold-curcumin: quaternary nanohybrid platform: a chemo/photothermal onco-strategy for improved cancer therapy. Carbohydr Polym Technol Appl. 2025;10:100795.
64. Othman Z, Mackey HR, Mahmoud KA. MXene/chitosan/lignosulfonate (MCL) nanocomposite for simultaneous removal of Co(II), Cr(VI), Cu(II), Ni(II) and Pb(II) heavy metals from wastewater. 2D Mater. 2023;10:024004.
65. Mahato P, Arshad F, Ali MS, Perera CS, Zou L. Removal of pharmaceutical compounds by chitosan nanocomposite membranes with catalytic additives from wastewater. Desalination. 2025;602:118635.
66. Rozmysłowska-Wojciechowska A, et al. Controlling the porosity and biocidal properties of the chitosan-hyaluronate matrix hydrogel nanocomposites by the addition of 2D Ti3C2Tx MXene. Materials. 2020;13:4587.
67. Ma T, Li L, Pan M, Guo C, Mei C. Multifunctional MXene-based fire alarm wallpaper with sandwich-like structure for enhanced fire safety and prevention. Chem Eng J. 2023;451:138517.
68. Wang C, et al. Ultra-impregnable MXene/ChNC@TiO2 membrane for oil/water microemulsion separation and photocatalytic degradation of dyes. Langmuir. 2025. https://doi.org/10.1021/ACS.LANGMUIR.5C01978.
69. Balasamy S, Ganapathy D, Atchudan R, Arya S, Sundramoorthy AK. Chitosan/MXene composite scaffolds for bone regeneration in oral cancer treatment - a review. Curr Cancer Ther Rev. 2024;21:1–14.
70. Iravani P, Iravani S, Varma RS. MXene-chitosan composites and their biomedical potentials. Micromachines. 2022;13:1383.
71. Zheng Y, Wang Y, Zhao J, Li Y. Electrostatic interfacial cross-linking and structurally oriented fiber constructed by surface-modified 2D MXene for high-performance flexible pseudocapacitive storage. ACS Nano. 2023;17:2487–96.
72. Pellis A, Guebitz GM, Nyanhongo GS. Chitosan: sources, processing and modification techniques. Gels. 2022;8:393.
73. Chen W, Cao P, Liu Y, Yu A, Wang D, Chen L, et al. Structural basis for directional chitin biosynthesis. Nature. 2022;610(7931):402–8.
74. Shamshina JL, Berton P, Rogers RD. Advances in functional chitin materials: a review. ACS Sustain Chem Eng. 2019;7:6444–57.
75. Yu A, Beck M, Merzendorfer H, Yang Q. Advances in understanding insect chitin biosynthesis. Insect Biochem Mol Biol. 2024;164:104058.
76. Kou S, Peters LM, Mucalo MR. Chitosan: a review of sources and preparation methods. Int J Biol Macromol. 2021;169:85–94.
77. Morgan K, Conway C, Faherty S, Quigley C. A comparative analysis of conventional and deep eutectic solvent (DES)-mediated strategies for the extraction of chitin from marine crustacean shells. Molecules. 2021;26:7603.
78. Kurita K. Chitin and chitosan: functional biopolymers from marine crustaceans. Mar Biotechnol. 2006;8:203–26.
79. Liu Y, et al. Chitin extraction from shrimp (*Litopenaeus vannamei*) shells by successive two-step fermentation with *Lactobacillus rhamnoides* and *Bacillus amyloliquefaciens*. Int J Biol Macromol. 2020;148:424–33.
80. Aranday-García R, Saimoto H, Shirai K, Ifuku S. Chitin biological extraction from shrimp wastes and its fibrillation for elastic nanofiber sheets preparation. Carbohydr Polym. 2019;213:112–20.
81. Castro R, Guerrero-Legarreta I, Bórquez R. Chitin extraction from *Allopetrolisthes punctatus* crab using lactic fermentation. Biotechnol Rep. 2018;20:e00287.
82. Deng JJ, et al. Enzymatic conversion and recovery of protein, chitin, and astaxanthin from shrimp shell waste. J Clean Prod. 2020;271:122655.
83. Govindan S, Nivethaa EAK, Saravanan R, Narayanan V, Stephen A. Synthesis and characterization of Chitosan–Silver nanocomposite. Appl Nanosci. 2012;2:299–303.
84. Sivanesan I, et al. Green synthesized chitosan/chitosan nanoforms/nanocomposites for drug delivery applications. Polymers. 2021;13:2256.
85. Rizeq BR, Younes NN, Rasool K, Nasrallah GK. Synthesis, bioapplications, and toxicity evaluation of chitosan-based nanoparticles. Int J Mol Sci. 2019;20:5776.
86. Novikov VY, Derkach SR, Konovalova IN, Dolgopyatova NV, Kuchina YA. Mechanism of heterogeneous alkaline deacetylation of chitin: a review. Polymers. 2023;15:1729.
87. Novikov VY, Konovalova IN, Dolgopyatova NV. The mechanism of chitin and chitosan deacetylation during long-term alkaline treatment. Appl Biochem Microbiol. 2022;58:309–14.
88. Sun X, Wang Y, Yu J, Wei Q, Ren X. Study on the deacetylation and mechanism of chitin in natural deep eutectic solvent. Int J Biol Macromol. 2024;255:127698.
89. Younes I, Rinaudo M. Chitin and chitosan preparation from marine sources. Structure, properties and applications. Mar Drugs. 2015;13:1133.
90. Aljawish A, Chevalot I, Jasniewski J, Scher J, Muniglia L. Enzymatic synthesis of chitosan derivatives and their potential applications. J Mol Catal B Enzym. 2015;112:25–39.
91. Kaczmarek MB, Struszczyk-Swita K, Li X, Szczęsna-Antczak M, Daroch M. Enzymatic modifications of chitin, chitosan, and chitooligosaccharides. Front Bioeng Biotechnol. 2019;7:481174.
92. Sivashankari PR, Prabaharan M. Deacetylation modification techniques of chitin and chitosan. Chitosan Based Biomater Fundamentals. 2017;1:117–33.
93. Suresh PV, Sachindra NM, Bhaskar N. Solid state fermentation production of chitin deacetylase by *Colletotrichum lindemuthianum* ATCC 56676 using different substrates. J Food Sci Technol. 2011;48:349–56.
94. Zhao Y, Park RD, Muzzarelli RAA. Chitin deacetylases: properties and applications. Mar Drugs. 2010;8:24–46.

95. Kalambate PK, et al. Recent advances in MXene–based electrochemical sensors and biosensors. TrAC Trends Anal Chem. 2019;120:115643.
96. Soundiraraju B, George BK. Two-dimensional titanium nitride (Ti2N) MXene: synthesis, characterization, and potential application as surface-enhanced raman scattering substrate. ACS Nano. 2017;11:8892–900.
97. Lim KRG, et al. Fundamentals of MXene synthesis. Nat Synth. 2022;1:601–14.
98. Vaia RA, et al. Halogen etch of Ti3AlC2 MAX phase for mxene fabrication. ACS Nano. 2021;15:2771–7.
99. Naguib M, et al. Two-dimensional nanocrystals produced by exfoliation of Ti3AlC2. Adv Mater. 2011;23:4248–53.
100. Zhan X, Si C, Zhou J, Sun Z. MXene and MXene-based composites: synthesis, properties and environment-related applications. Nanoscale Horiz. 2020;5:235–58.
101. Vahidmohammadi A, Hadjikhani A, Shahbazmohamadi S, Beidaghi M. Two-dimensional vanadium carbide (MXene) as a high-capacity cathode material for rechargeable aluminum batteries. ACS Nano. 2017;11:11135–44.
102. Naguib M, et al. New two-dimensional niobium and vanadium carbides as promising materials for li-ion batteries. J Am Chem Soc. 2013;135:15966–9.
103. Halim J, et al. Synthesis and characterization of 2D molybdenum carbide (MXene). Adv Funct Mater. 2016;26:3118–27.
104. Sang X, et al. Atomic defects in monolayer titanium carbide (Ti3C2Tx) MXene. ACS Nano. 2016;10:9193–200.
105. Arole K, et al. Water-dispersible Ti3C2Tz MXene nanosheets by molten salt etching. iScience. 2021;24:103403.
106. Liu L, et al. Exfoliation and delamination of Ti3C2TxMXene prepared via molten salt etching route. ACS Nano. 2022;16:111–8.
107. Jiang L, et al. 2D single- and few-layered MXenes: synthesis, applications and perspectives. J Mater Chem A. 2022;10:13651–72.
108. Turker F, et al. CVD synthesis and characterization of thin Mo2C crystals. J Am Ceram Soc. 2020;103:5586–93.
109. Xu C, et al. Large-area high-quality 2D ultrathin Mo2C superconducting crystals. Nat Mater. 2015;14:1135–41.
110. GengD, Zhao X, Chen Z, Sun W, Fu W, Chen J, Liu W, Zhou W, Loh KP. Direct synthesis of large-area 2D Mo_2C on in situ grown graphene. Adv Mater. 2017;29(35):1700072 https://doi.org/10.1002/adma.201700072.
111. Kondawar SB, Modak PR. Theory of EMI shielding. In: Kuruvilla J, Runcy W, Gejo G, editors. Materials for Potential EMI Shielding Applications Processing Properties and Current Trends. Elsevier; 2020.
112. Wang H, Li S, Liu M, Li J, Zhou X. Review on shielding mechanism and structural design of electromagnetic interference shielding composites. Macromol Mater Eng. 2021;306:2100032.
113. Liu J, et al. Hydrophobic, flexible, and lightweight MXene foams for high-performance electromagnetic-interference shielding. Adv Mater. 2017;29:1702367.
114. Liu J, et al. Magnetic, electrically conductive and lightweight graphene/iron pentacarbonyl porous films enhanced with chitosan for highly efficient broadband electromagnetic interference shielding. Compos Sci Technol. 2017;151:71–8.
115. Wang L, et al. Current advances and future perspectives of MXene-based electromagnetic interference shielding materials. Adv Compos Hybrid Mater. 2023;6:1–18.
116. Verma R, Thakur P, Chauhan A, Jasrotia R, Thakur A. A review on MXene and its' composites for electromagnetic interference (EMI) shielding applications. Carbon N Y. 2023;208:170–90.
117. Iqbal A, Sambyal P, Koo CM. 2D MXenes for electromagnetic shielding: a review. Adv Funct Mater. 2020;30:2000883.
118. Wang C, et al. Polyvinyl alcohol /chitosan biomimetic hydrogel enhanced by MXene for excellent electromagnetic shielding and pressure sensing. Int J Biol Macromol. 2024;278:134354.
119. Jalali A, et al. Lightweight 3D-printed chitosan/MXene aerogels for advanced electromagnetic shielding, energy harvesting, and thermal management. Carbohydr Polym. 2025;352:123252.
120. Wang X, et al. Disulfide bond network crosslinked flexible multifunctional chitosan coating on fabric surface prepared by the chitosan grafted with thioctic acid. Int J Biol Macromol. 2024;263:130431.
121. Ganguly S, et al. Mussel-inspired polynorepinephrine/MXene-based magnetic nanohybrid for electromagnetic interference shielding in X-band and strain-sensing performance. Langmuir. 2022;38:3936–50.
122. Das P, Rosenkranz A, Ganguly S. MXene Nanocomposites: Design, Fabrication, and Shielding Applications. In: Das P, Rosenkranz A, Ganguly S, editors. MXene Nanocomposites: Design, Fabrication, and Shielding Applications. CRC Press; 2023.
123. Eghbali P, et al. Recent advances in design and engineering of MXene-based catalysts for photocatalysis and persulfate-based advanced oxidation processes: a state-of-the-art review. Chem Eng J. 2024;480:147920.
124. Shelly D, Jin FL, Lee SY, Park SJ. Emerging trends in MXene-polymer composites for electromagnetic shielding applications. Compos Commun. 2024;51:102056.
125. Sanandiya ND, et al. Chitosan-based electroconductive inks without chemical reaction for cost-effective and versatile 3D printing for electromagnetic interference (EMI) shielding and strain-sensing applications. Carbohydr Polym. 2024;337:122161.
126. Shi X, et al. Scalable, high-yield monolayer MXene preparation from multilayer MXene for many applications. Angew Chem Int Ed Engl. 2025;64:e202418420.
127. Tan Z, et al. Fabrication of chitosan/MXene multilayered film based on layer-by-layer assembly: toward enhanced electromagnetic interference shielding and thermal management capacity. Compos Part A Appl Sci Manuf. 2022;155:106809.
128. Wu S, et al. Ultralight and hydrophobic MXene/chitosan-derived hybrid carbon aerogel with hierarchical pore structure for durable electromagnetic interference shielding and thermal insulation. Chem Eng J. 2022;446:137093.
129. Liu F, et al. Well-aligned MXene/chitosan films with humidity response for high-performance electromagnetic interference shielding. Carbohydr Polym. 2020;243:116467.
130. Ouyang W, et al. Ultrathin-flexible multifunctional MXene composite hydrogels with good mechanical properties-high strain sensitivity and ultra-broadband EMI shielding performances. Chem Eng J. 2024;494:153068.
131. Pei X, et al. 3D-printing carbon nanotubes/Ti3C2Tx/chitosan composites with different arrangement structures based on ball milling for EMI shielding. J Appl Polym Sci. 2022;139:e53125.
132. Han W, Huang K, Yu Q, Yi L, Chen D. Electrostatic interaction-inspired textiles based on MXene decoration for superior electromagnetic interference shielding, infrared thermal camouflage, and fire proofing. Colloids Surf A Physicochem Eng Asp. 2025;718:136934.
133. Mei L, et al. Super tough multifunctional MXene/PAA-CS double network hydrogels with high mechanical sensing properties and excellent EMI shielding performance. Small. 2025;21:2410687.

134. Peng Q, et al. The synergistic effect of hybridization-micro/nano-structural design on the Ti_3C_2Tx MXene@CoFe-MOF@chitosan heterojunction enhances the absorption of electromagnetic waves. Adv Compos Hybrid Mater. 2025;8:1–14.
135. Xie K, et al. Application of two-dimensional MXene materials in sensors. Mater Des. 2023;228:111867.
136. Zahra QulA, et al. MXene-based aptasensors: advances, challenges, and prospects. Prog Mater Sci. 2022;129:100967.
137. Wu L, et al. MXene sensors based on optical and electrical sensing signals: from biological, chemical, and physical sensing to emerging intelligent and bionic devices. PhotoniX. 2023;4:1–56.
138. Wu X, et al. Application of MXene in electrochemical sensors: a review. Electroanalysis. 2021;33:1827–51.
139. Manasa G, Rout CS. Versatile MXenes as electrochemical sensors for heavy metal ions and phenolic moiety-containing industrial chemicals: recent development and prospects. Mater Adv. 2024;5:83–122.
140. Yang H, et al. Topographic design in wearable MXene sensors with in-sensor machine learning for full-body avatar reconstruction. Nat Commun. 2022;13:1–15.
141. Zhao Z, et al. Recent advances in MXene-based electrochemical sensors. Biosensors. 2025;15:107.
142. Rhouati A, Berkani M, Vasseghian Y, Golzadeh N. MXene-based electrochemical sensors for detection of environmental pollutants: a comprehensive review. Chemosphere. 2022;291:132921.
143. Tong X, et al. Highly stable glucose oxidase polynanogel@MXene/chitosan electrochemical biosensor based on a multistable interface structure for glucose detection. Biosens Bioelectron. 2024;248:115942.
144. Ni Y, Chen J, Chen K. Flexible vanillin-polyacrylate/chitosan/mesoporous nanosilica-MXene composite film with self-healing ability towards dual-mode sensors. Carbohydr Polym. 2024;335:122042.
145. Gu M, et al. High-sensitivity, ultrawide linear range, antibacterial textile pressure sensor based on chitosan/MXene hierarchical architecture. iScience. 2024;27:109481.
146. Zhang H, et al. Preparation of self-healing MXene/chitosan/benzaldehyde-polyurethane flexible conductive coating for dual-mode sensing applications. Compos Part B Eng. 2024;287:111875.
147. Yang Z, Li H, Zhang S, Lai X, Zeng X. Superhydrophobic MXene@carboxylated carbon nanotubes/carboxymethyl chitosan aerogel for piezoresistive pressure sensor. Chem Eng J. 2021;425:130462.
148. Zhao Y, et al. Highly sensitive, wearable piezoresistive methylcellulose/chitosan@MXene aerogel sensor array for real-time monitoring of physiological signals of pilots. Sci China Mater. 2025;68:542–51.
149. Liu Z, et al. A wearable 3D pressure sensor based on electrostatic self-assembly MXene/chitosan sponge and insulating PVP spacer. Nanotechnology. 2023;34:455502.
150. Li XP, et al. Highly sensitive, reliable and flexible piezoresistive pressure sensors featuring polyurethane sponge coated with MXene sheets. J Colloid Interface Sci. 2019;542:54–62.
151. Lu H, et al. Biobased, degradable and directional porous carboxymethyl chitosan/lignosulfonate sodium aerogel-based piezoresistive pressure sensor with dual-conductive network for human motion detection. Chem Eng J. 2024;497:154868.
152. He X, Zhang L, Lu X, Zhang A, Zhang J. Carboxymethyl chitosan synergistically enhanced MXene composite aerogel for piezoresistive sensors and thermal management. Ind Eng Chem Res. 2024;63:15901–11.
153. Liu M, Liu X, Yang F. Flexible and washable MXene@PEDOT:PSS@CS@PU pressure sensors. Sens Actuators A Phys. 2024;378:115810.
154. Shang C, et al. One 3D aerogel wearable pressure sensor with ultrahigh sensitivity, wide working range, low detection limit for voice recognition and physiological signal monitoring. Sci China Mater. 2023;66:1911–22.
155. Xie J, et al. Knitted fabric-based flexible piezoresistive pressure sensors for human monitoring and underwater emergency rescue. Sens Actuators A Phys. 2025;382:116183.
156. Liu Y, et al. High-performance lightweight and flexible PVDF-B/MXene/Chitosan composite aerogel for sensitive self-powered sensing. ACS Appl Polym Mater. 2024. https://doi.org/10.1021/acsapm.4c01731.
157. Yong Y, et al. Wide-Range and Sensitive Piezoresistive Sensor Based on Chitosan-Modified Polyurethane Foam-Coated MXene Nanosheets. ACS Appl Nano Mater. 2025. https://doi.org/10.1021/acsanm.5c00146.
158. Wang T, et al. PVA/chitosan-based multifunctional hydrogels constructed through multi-bonding synergies and their application in flexible sensors. Carbohydr Polym. 2025;350:123034.
159. Xu B, et al. Self-healing PVA/Chitosan/MXene triple network hydrogel for strain and temperature sensors. Int J Biol Macromol. 2025;290:138811.
160. Hu Y, et al. Biomass polymer-assisted fabrication of aerogels from MXenes with ultrahigh compression elasticity and pressure sensitivity. J Mater Chem A Mater. 2019;7:10273–81.
161. Li SN, et al. Environmentally stable, mechanically flexible, self-adhesive, and electrically conductive Ti3C2TX MXene hydrogels for wide-temperature strain sensing. Nano Energy. 2021;90:106502.
162. Xu H, Zhang J, Lu X, Feng S, Xu Z. Ionic liquid-assisted stabilization of MXene in polysaccharide-chitosan hydrogels with mechanical enhancement for catalytic and sensor applications. Int J Biol Macromol. 2025;310:143466.
163. Huang M, et al. Multimodal sensing conductive organohydrogel electronics based on chitosan-encapsulated MXene nanocomposites for deep learning-enhanced ball sports recognition. Soft Sci. 2025;5:24.
164. Shekh MI, et al. Dynamically bonded, tough, and conductive MXene@oxidized sodium alginate: chitosan based multi-networked elastomeric hydrogels for physical motion detection. Int J Biol Macromol. 2023;224:604–20.
165. Li X, et al. Onion-inspired MXene/chitosan-quercetin multilayers: enhanced response to H2O molecules for wearable human physiological monitoring. Sens Actuators B Chem. 2021;329:129209.
166. Liu T, et al. MXene/TPU composite film for humidity sensing and human respiration monitoring. Adv Sens Res. 2024;3:2300014.
167. Li Y, Huang X, Chen Q, Yao Y, Pan W. Nanochitin/MXene composite coated on quartz crystal microbalance for humidity sensing. Nanomaterials. 2023;13:3135.
168. Xiao Y, et al. Ti3C2Tx aerogel-based wearable humidity sensors with low hysteresis and high linearity for expiratory comfort management. ACS Sens. 2024. https://doi.org/10.1021/acssensors.4c02338.
169. Wang X, Li M, Yang S, Shan J. A novel electrochemical sensor based on TiO2–Ti3C2TX/CTAB/chitosan composite for the detection of nitrite. Electrochim Acta. 2020;359:136938.
170. Yin J, et al. Highly sensitive non-invasive glucose sensing based on chitosan-coated MXene/NiCo-LDH composites. J Electroanal Chem. 2025;984:119064.
171. Hu T, et al. Free-standing MXene/chitosan/Cu2O electrode: an enzyme-free and efficient biosensor for simultaneous determination of glucose and cholesterol. J Zhejiang Univ Sci A. 2022;23:579–86.

172. Song D, et al. Metal–organic frameworks-derived MnO2/Mn3O4 microcuboids with hierarchically ordered nanosheets and Ti3C2 MXene/Au NPs composites for electrochemical pesticide detection. J Hazard Mater. 2019;373:367–76.
173. Wu L, et al. 2D transition metal carbide MXene as a robust biosensing platform for enzyme immobilization and ultrasensitive detection of phenol. Biosens Bioelectron. 2018;107:69–75.
174. Zhang L, et al. A polyoxometalate/chitosan-Ti3C2Tx MXene nanocomposite constructed by electrostatically mediated strategy for electrochemical detecting L-tryptophan in milk. Food Chem. 2024;458:140309.
175. Wang Z, et al. Construction of Ti3C2Tx/CMCS cross-linked molecularly imprinted electrochemical sensor and its ultrasensitive detection of ciprofloxacin. Chem Eng J. 2025;519:165213.
176. Isailović J, et al. Study of chitosan-stabilized Ti3C2Tx MXene for ultrasensitive and interference-free detection of gaseous H2O2. ACS Appl Mater Interfaces. 2023;15:31643–51.
177. Hu X, et al. Superassembled MXene–carboxymethyl chitosan nanochannels for the highly sensitive recognition and detection of copper ions. Analyst. 2024;149:1464–72.
178. Dago-Serry Y, Maroulas KN, Tolkou AK, Kokkinos NC, Kyzas GZ. How the chitosan structure can affect the adsorption of pharmaceuticals from wastewaters: an overview. Carbohydr Polym Technol Appl. 2024;7:100466.
179. Janjhi FA, et al. MXene-based materials for removal of antibiotics and heavy metals from wastewater– a review. Water Resour Indus. 2023;29:100202.
180. Ren CE, et al. Charge- and size-selective ion sieving through Ti3C2Tx MXene membranes. J Phys Chem Lett. 2015;6:4026–31.
181. Yang H, et al. High performance mixed-dimensional assembled MXene composite membranes for molecular sieving. J Memb Sci. 2024;698:122606.
182. Mahato P, Mcelhinney J, Jarusheh HS, Palmisano G, Zou L. Laccase/chitosan/MXene/GO catalytic composite membrane for highly effective fouling resistance. Desalination. 2025;599:118443.
183. Ding H, et al. Synthesis of CS/Fe3O4/TiO2@MXene nanocomposite photocatalyst with excellent degradation and bacteriostatic properties by one-step hydrothermal method. Ceram Int. 2024;50:46334–46.
184. Wang R, et al. Construction of alkalized MXene-supported CoFe2O4/CS composites with super-strong adsorption capacity to remove toxic dyes from aqueous solution. Appl Surf Sci. 2023;624:157091.
185. Qiang T, Qiu B, Chen L, Ren L. Carboxylated chitosan modified alkalization of 2D MXene Ti3C2 and its Cr(VI) removal performance in aqueous solution. Ceram Int. 2023;49:6688–98.
186. Lin J, et al. MXene/ZnS/chitosan-cellulose composite with Schottky heterostructure for efficient removal of anionic dyes by synergistic effect of adsorption and photocatalytic degradation. Int J Biol Macromol. 2024;269:131994.
187. Ijaz I, et al. Functionalization of chitosan biopolymer using two dimensional metal-organic frameworks and MXene for rapid, efficient, and selective removal of lead (II) and methyl blue from wastewater. Process Biochem. 2023;129:257–67.
188. Yu C, Nghiem LD, Zou L. Catalytic chitosan/MXene/GO nanocomposite membrane for removing dye and heavy metals. Desalination. 2025;594:118313.
189. Wu Z, et al. Pod-inspired MXene/porous carbon microspheres with ultrahigh adsorption capacity towards crystal violet. Chem Eng J. 2021;426:130776.
190. Xu J, et al. Application of 3D magnetic nanocomposites: MXene-supported Fe3O4@CS nanospheres for highly efficient adsorption and separation of dyes. Sci Total Environ. 2022;822:153544.
191. Qin Y, et al. Chitosan-integrated MXene-based nanofiltration membrane with high permeability for efficient dye wastewater treatment. J Appl Polym Sci. 2025;142:e57157.
192. Xing C, et al. Efficient water purification using stabilized MXene nanofiltration membrane with controlled interlayer spacings. Sep Purif Technol. 2023;317:123774.
193. Alyasi H, Wahib S, Tong Y, Gomez T, Mahmoud KA. Magnetic MXene chitosan-lignosulfonate composite (Fe3O4@ MCLS) for the reductive removal of Cr(VI) and other heavy metals from water. J Hazard Mater Adv. 2025;17:100536.
194. Yang G, et al. Surface functionalization of MXene with chitosan through in-situ formation of polyimidazoles and its adsorption properties. J Hazard Mater. 2021;419:126220.
195. Wan H, Nan L, Geng H, Zhang W, Shi H. Green synthesis of a novel MXene–CS composite applied in treatment of Cr(VI) contaminated aqueous solution. Processes. 2021;9:524.
196. Azeez NR, Salih SS, Kadhom M, Mohammed HN, Ghosh TK. Enhanced termination of zinc and cadmium ions from wastewater employing plain and chitosan-modified mxenes: synthesis, characterization, and adsorption performance. Green Chem Eng. 2024;5:339–47.
197. Nezami S, Ghaemi A, Yousefi T. The potential of Ti3C2Tx-KH2PO4 and Ti3C2Tx-chitosan in the efficient removal of cesium from nuclear wastewater. Sci Rep. 2024;14:1–21.
198. Asif UA, Mahmood K, Naqvi SR, Mehran MT, Noor T. Development of high-capacity surface-engineered MXene composite for heavy metal Cr (VI) removal from industrial wastewater. Chemosphere. 2023;326:138448.
199. Liu F, Si L, Hu B. Constructing 3D magnetic MXenes/chitosan composites to reinforce U(VI) and Cr(VI) trapping: excavating from performance to mechanism. Sep Purif Technol. 2025;352:128094.
200. Bukhari A, et al. Simultaneous removal of Norfloxacin, Ciprofloxacin, and copper from aqueous solution by chitosan and MXene functionalized graphene oxide ternary composite based on anion-synergistic interaction. Chem Eng J. 2023;474:145890.
201. Arshad F, Ali MS, Ali L, Zou L. Catalytic MnO2/MXene/chitosan nanocomposite membrane in removing caffeine from wastewater. Sep Purif Technol. 2025;361:131504.
202. Li Y, et al. Efficient removal of antibiotics from wastewater by chitosan/polyethyleneimine/Ti3C2 MXene composite hydrogels: synthesis, adsorption, kinetics and mechanisms. Colloids Surf A Physicochem Eng Asp. 2024;702:135111.
203. Chen J, et al. Ti3C2TX-Co loaded chitosan hydrogel microspheres for efficient peroxymonosulfate activation and tetracycline degradation. Sep Purif Technol. 2025;354:129249.
204. Shanthini K, et al. Designing Ti3C2/C3N4-embedded chitosan nanocomposites for efficient antibiotic degradation and antibacterial activity. Opt Mater. 2024;147:114731.
205. Wu Z, et al. Chitosan assisted MXene decoration onto polymer fabric for high efficiency solar driven interfacial evaporation of oil contaminated seawater. J Colloid Interface Sci. 2022;622:169–80.
206. Raza W, et al. Recent advancements in supercapacitor technology. Nano Energy. 2018;52:441–73.

207. Karthikeyan S, Narenthiran B, Sivanantham A, Bhatlu LD, Maridurai T. Supercapacitor: evolution and review. Mater Today: Proc. 2021;46:3984–8.
208. Şahin ME, Blaabjerg F, Sangwongwanich A. A comprehensive review on supercapacitor applications and developments. Energies. 2022;15:674.
209. Panda S, et al. MXene based emerging materials for supercapacitor applications: recent advances, challenges, and future perspectives. Coord Chem Rev. 2022;462:214518.
210. Zheng W, Halim J, Persson POÅ, Rosen J, Barsoum MW. MXene-based symmetric supercapacitors with high voltage and high energy density. Mater Rep Energy. 2022;2:100078.
211. Wang X, et al. A renewable hydrogel electrolyte membrane prepared by carboxylated chitosan and polyacrylamide for solid-state supercapacitors with wide working temperature range. J Power Sources. 2023;560:232704.
212. Al-Farraj ES, et al. Fabrication of hybrid nanocomposite derived from chitosan as efficient electrode materials for supercapacitor. Int J Biol Macromol. 2018;120:2271–8.
213. Chen F, et al. High surface area porous carbon derived from chitosan: CH3COOH/(NH4)2HPO4 dual-assisted hydrothermal carbonization synthesis and its application in supercapacitor. J Energy Storage. 2023;71:108180.
214. Ding Y, et al. Three-dimensional ordered and porous Ti3C2Tx@Chitosan film enabled by self-assembly strategy for high-rate pseudocapacitive energy storage. Chem Eng J. 2022;442:136255.
215. Cui Y, et al. MXene/biomass/chitosan carbon aerogel (MBC) with shared cathode and anode for the construction of high-efficiency asymmetric supercapacitor. Chem Eng J. 2023;472:144701.
216. Wei L, et al. Sandwich-like chitosan porous carbon spheres/MXene composite with high specific capacitance and rate performance for supercapacitors. J Bioresour Bioprod. 2022;7:63–72.
217. Pu L, et al. N-doped MXene derived from chitosan for the highly effective electrochemical properties as supercapacitor. Adv Compos Hybrid Mater. 2022;5:356–69.
218. Zhu C, Geng F. Macroscopic MXene ribbon with oriented sheet stacking for high-performance flexible supercapacitors. Carbon Energy. 2021;3:142–52.
219. Yu T, Ge S, Hu M, Wu H, Yao S. A novel CoS/Ti3C2Tx MXene conductive filler effectively improves the pseudocapacitive performance of conductive hydrogel electrode materials for all-solid-state supercapacitors. Eur Polym J. 2024;209:112904.
220. Yu T, Lei X, Fan K, Chen H, Liu J. Poly (acrylic acid)/Chitosan hydrogel with excellent self-healing properties for supercapacitor electrodes using PbS/Ti3C2Tx heterostructure as conductive fillers. Int J Hydrogen Energy. 2024;50:1122–32.
221. Yu T, Lei X, Zhou Y, Chen H. Ti3C2Tx MXenes reinforced PAA/CS hydrogels with self-healing function as flexible supercapacitor electrodes. Polym Adv Technol. 2021;32:3167–79.
222. Tamilselvi S, et al. A review on battery modelling techniques. Sustainability. 2021;13:10042.
223. Worku AK, Alemu MA, Ayele DW, Getie MZ, Teshager MA. Recent advances in MXene-based materials for high-performance metal-air batteries. Green Chem Lett Rev. 2024. https://doi.org/10.1080/17518253.2024.2325983.
224. Zhang Y, et al. Adjustable MXene-based materials in metal-ion batteries: progress, prospects, and challenges. Small Struct. 2024;5:2300255.
225. Liu H, et al. Versatile MXenes for aqueous zinc batteries. Adv Sci. 2024;11:2305806.
226. Zhu J, et al. VS4 anchored on Ti3C2 MXene as a high-performance cathode material for magnesium ion battery. J Power Sour. 2022;518:230731.
227. Chen C, et al. Customizing hydrophilic terminations for V2CTx MXene toward superior hybrid-ion storage in aqueous zinc batteries. Adv Funct Mater. 2024;34:2308508.
228. Tan L, et al. Long-life and dendrite-free zinc metal anode enabled by a flexible, green and self-assembled zincophilic biomass engineered MXene based interface. Chem Eng J. 2022;431:134277.
229. Bashir T, et al. Progress in 3D-MXene electrodes for lithium/sodium/potassium/magnesium/zinc/aluminum-ion batteries. Electrochem Energ Rev. 2023;6:1–34.
230. Wu M, et al. A sustainable chitosan-zinc electrolyte for high-rate zinc-metal batteries. Matter. 2022;5:3402–16.
231. Chen Y, et al. Chitosan as a functional additive for high-performance lithium–sulfur batteries. J Mater Chem A Mater. 2015;3:15235–40.
232. Bargnesi L, Gigli F, Albanelli N, Toigo C, Arbizzani C. Crosslinked chitosan binder for sustainable aqueous batteries. Nanomaterials. 2022;12:254.
233. Prasanna K, et al. Chitosan complements entrapment of silicon inside nitrogen doped carbon to improve and stabilize the capacity of Li-ion batteries. Sci Rep. 2019;9:1–13.
234. Li X, et al. Constructing Si@CN@MXene from silicon waste as high-performance lithium-ion battery anodes. Diam Relat Mater. 2024;148:111493.
235. Xu J, et al. Chitosan derived nitrogen and oxygen dual-doped hierarchical porous carbon/Ti3C2Tx MXene fiber for flexible cable shaped lithium-selenium battery. Int J Biol Macromol. 2024;282:136836.
236. Shi C, et al. A hierarchical porous carbon aerogel embedded with small-sized TiO2 nanoparticles for high-performance Li–S batteries. Carbon. 2023;202:59–65.
237. Li X, et al. V2CTX MXene sphere for aqueous ion storage. Energy Mater Adv. 2023. https://doi.org/10.34133/energymatadv.0066.
238. Wang Y, Zheng Y, Zhao J, Li Y. Assembling free-standing and aligned tungstate/MXene fiber for flexible lithium and sodium-ion batteries with efficient pseudocapacitive energy storage. Energy Storage Mater. 2020;33:82–7.
239. Wang Y-J, et al. Recent progress on MXene-based advanced nanocomposite materials for thermal radiation protection and fire safety. Adv Nanocomp. 2024;1:217–39.
240. Mao M, et al. Facile and green fabrication of flame-retardant Ti3C2Tx MXene networks for ultrafast, reusable and weather-resistant fire warning. Chem Eng J. 2022;427:131615.
241. Goel N, Kushwaha A, Kumar M. Two-dimensional MXenes: recent emerging applications. RSC Adv. 2022;12:25172–93.
242. Rong C, et al. Elastic properties and tensile strength of 2D Ti3C2Tx MXene monolayers. Nat Commun. 2024;15:1–8.
243. Hatam-Lee SM, Esfandiar A, Rajabpour A. Mechanical behaviors of titanium nitride and carbide MXenes: a molecular dynamics study. Appl Surf Sci. 2021;566:150633.
244. Chen M, et al. Recent advancements of bio-derived flame retardants for polymeric materials. Polymers. 2025;17:249.
245. Wu R, Wang Y, Liu Y, Yuan B. Functionalizing chitosan-based film with highly sensitive fire response and commendable flame retardancy for intelligent fire-alarm system. Compos Part A Appl Sci Manuf. 2024;178:107999.

246. Chen R, et al. Synthesis of chitosan-based flame retardant and its fire resistance in epoxy resin. Carbohydr Polym. 2020;245:116530.
247. Liu L, et al. Phosphorylated chitosan@MXene biomass-based coating with high flame retardancy and environmental friendliness for cotton fabric. Int J Biol Macromol. 2025;301:140344.
248. Ma T, et al. Nacre-inspired intumescent flame retardant bridging network for intelligent fire warning and prevention. Chem Eng J. 2023;468:143786.
249. Yang F, et al. Expeditious self-healing supermolecules enabling fireproof and ultra-long-life of intelligent bamboo fire alarm systems. Ind Crops Prod. 2025;224:120391.
250. He X, et al. Synergistic effect of GO and MXene enables ultrasensitive, reversible, and self-powered fire warning of a GO/MXene/chitosan aerogel. ACS Appl Mater Interfaces. 2024. https://doi.org/10.1021/acsami.4c13774.
251. He Y, Wen J, Huang J, Gan L. Multifunctional enhancement strategy for MXene-based fire alarm sensors via interlocked "brick/mortar" structure of dimension-hybrid nanoparticle system. J Mater Res Technol. 2024;33:8142–50.
252. Cao F, et al. Preparation of a multifunctional soybean protein isolate-based adhesive with enhanced mechanical and flame retardancy properties via the synergistic effect between phosphorylated chitosan and quaternary ammonium-functionalized MXene. Int J Biol Macromol. 2025;296:139684.
253. Lin B, et al. Experimental and numerical perspective on the fire performance of MXene/Chitosan/Phytic acid coated flexible polyurethane foam. Sci Rep. 2021;11:1–13.
254. Wang B, et al. Multifunctional MXene/Chitosan-coated cotton fabric for intelligent fire protection. ACS Appl Mater Interfaces. 2021;13:23020–9.
255. Li SN, et al. Mechanically flexible and flame-retardant cellulose nanofibril-based films integrated with MXene and chitosan. Soft Sci. **2**, N/A-N/A (2022).
256. Lin B, et al. MXene/chitosan nanocoating for flexible polyurethane foam towards remarkable fire hazards reductions. J Hazard Mater. 2020;381:120952.
257. Lin B, et al. Dual functionalisation of polyurethane foam for unprecedented flame retardancy and antibacterial properties using layer-by-layer assembly of MXene chitosan with antibacterial metal particles. Compos Part B Eng. 2022;244:110147.
258. Luo Y, et al. Fabrication of thermoplastic polyurethane with functionalized MXene towards high mechanical strength, flame-retardant, and smoke suppression properties. J Colloid Interface Sci. 2022;606:223–35.
259. Voutchkov N. Energy use for membrane seawater desalination – current status and trends. Desalination. 2018;431:2–14.
260. Ihsanullah I. Potential of MXenes in water desalination: current status and perspectives. Nanomicro Lett. 2020;12:1–20.
261. Su J, et al. MXene-based flexible and washable photothermal fabrics for efficiently continuous solar-driven evaporation and desalination of seawater. Renew Energy. 2022;195:407–15.
262. Sreedhar A, Noh JS. Advancements in solar desalination of seawater by various Ti3C2 MXene based morphologies for freshwater generation: a review. Catalysts. 2021;11:1435.
263. Sapna S, Sharma R, Kumar D. Chitosan-Based Membranes for Wastewater Desalination and Heavy Metal Detoxification. In: Thomas S, Pasquini D, Shao-Yuan L, Gopakumar DA, editors. Nanoscale Materials in Water Purification. Elsevier; 2019.
264. Al-Manhel AJ, Al-Hilphy ARS, Niamah AK. Extraction of chitosan, characterisation and its use for water purification. J Saudi Soc Agric Sci. 2018;17:186–90.
265. Liu Q, Xiao W, Liao B, Yan K, Zhang J. Chitosan aerogel-carbon nanotubes double layer solar evaporator for efficient desalination. Chem Eng J Adv. 2022;10:100260.
266. Sun M, et al. Wood-inspired anisotropic PU/chitosan/MXene aerogel used as an enhanced solar evaporator with superior salt-resistance. Desalination. 2023;555:116462.
267. Chen S, et al. Multifunctional super-hydrophilic MXene/biomass composite aerogel evaporator for efficient solar-driven desalination and wastewater treatment. Small. 2024;20:2400603.
268. Zhang F, Qi Z, Han X, Cai H, Yang K. MXene nanosheet-reinforced chitosan as a stable photothermal evaporator for efficient solar evaporation. Sustain Energy Fuels. 2024;8:3680–7.
269. Zhang G, Zhang Y, Jiang J. Robust and multifunctional MXene/rGO composite aerogels toward highly efficient solar-driven interfacial evaporation and wastewater treatment. Sep Purif Technol. 2024;347:127588.
270. Sun J, et al. Hydrogel-based photothermal-catalytic membrane for efficient cogeneration of freshwater and hydrogen in membrane distillation system. Adv Funct Mater. 2025. https://doi.org/10.1002/adfm.202416768.
271. Hao S, et al. Fabrication of chitosan-based hydrogel embedded with antibacterial AgMXene nanocomposites as photothermal centers for solar steam generation and purification. ACS Appl Energy Mater. 2024;7:1250–60.
272. Hao S, Chen X, Zhao T, et al. Fabrication of antibacterial and biomimetic chitosan-based hydrogel embedded with Ag/MXene nanocomposites as photothermal centers for solar steam generation and desalination. Authorea Preprints; 2023.
273. Fan D, et al. Synergy of photocatalysis and photothermal effect in integrated 0D perovskite oxide/2D MXene heterostructures for simultaneous water purification and solar steam generation. Appl Catal B Environ. 2021;295:120285.
274. Jin Y, He Y, Wang H, Li S, Liu J. Chitosan/multilayered MXene nanocomposites loaded in 3D nitrogen-doped carbon networks for seawater desalination with highly efficient photothermal conversion. Adv Sustain Syst. 2023;7:2300056.
275. Wang Y, et al. Bio-inspired MXene coated wood-like ordered chitosan aerogels for efficient solar steam generating devices. J Mater Sci. 2022;57:13962–73.
276. Jin L, et al. Large-scale carbon fiber-based solar-driven evaporator with 1T MoS2-MXene heterostructure: towards reliable mechanical performance and efficient seawater desalination. Chem Eng J. 2024;497:154469.
277. Goyal P, Sundarrajan S, Ramakrishna S. A review on mixed matrix membranes for solvent dehydration and recovery process. Membranes. 2021;11:441.
278. Castro-Muñoz R. MXene: a two-dimensional material in selective water separation via pervaporation. Arab J Chem. 2022;15:103524.
279. Liu G, et al. Two-dimensional Ti2CTx MXene membranes with integrated and ordered nanochannels for efficient solvent dehydration. J Mater Chem A. 2019;7:12095–104.
280. Liu C, Wang G, Sui W, An L, Si C. Preparation and characterization of chitosan by a novel deacetylation approach using glycerol as green reaction solvent. ACS Sustain Chem Eng. 2017;5:4690–8.
281. Castro-Muñoz R, et al. Hybrid cross-linked chitosan/protonated-proline:glucose DES membranes with superior pervaporation performance for ethanol dehydration. J Mol Liq. 2022;360:119499.

282. Han YJ, Wang KH, Lai JY, Liu YL. Hydrophilic chitosan-modified polybenzoimidazole membranes for pervaporation dehydration of isopropanol aqueous solutions. J Memb Sci. 2014;463:17–23.
283. Xu Z, Liu G, Ye H, Jin W, Cui Z. Two-dimensional MXene incorporated chitosan mixed-matrix membranes for efficient solvent dehydration. J Memb Sci. 2018;563:625–32.
284. Wang L, Shi B. Hydroxide conduction enhancement of chitosan membranes by functionalized MXene. Materials. 2018;11:2335.
285. Munshi MH, et al. Transparent and flexible MXene-chitosan nanocomposite film for effective UV and high-energy blue light shielding applications. RSC Sustain. 2025. https://doi.org/10.1039/D5SU00271K.
286. Deshmukh K, Muzaffar A, Kovárík T, Ahamed MB, Pasha SKK. Introduction to 2D MXenes fundamental aspects, MAX phases and MXene derivatives current challengesand future prospects. In: Kishor KS, Kalim D, Khadheer Pasha SK, Tomáš K, editors. MXenes and their Composites Synthesis Properties and Potential Applications. Elsevier; 2022.
287. Hossaın MT, Repon MR, Shahid MA, Ali A, Islam T. Progress, prospects and challenges of MXene integrated optoelectronics devices. ChemElectroChem. 2024;11:e202400008.
288. Nahirniak S, Ray A, Saruhan B. Challenges and future prospects of the MXene-based materials for energy storage applications. Batteries. 2023;9:126.
289. Khatami M, Iravani S. MXenes and MXene-based materials for the removal of water pollutants: challenges and opportunities. Comments Inorg Chem. 2021;41:213–48.
290. Xia Q, et al. MXene-based chemical gas sensors: recent developments and challenges. Diam Relat Mater. 2023;131:109557.
291. Awan HTA, Kumar L, Wong WP, Walvekar R, Khalid M. Recent progress and challenges in MXene-based phase change material for solar and thermal energy applications. Energies. 2023;16:1977.
292. Prabhakar Vattikuti SV, Shim J, Rosaiah P, Mauger A, Julien CM. Recent advances and strategies in MXene-based electrodes for supercapacitors: applications, challenges and future prospects. Nanomaterials. 2023;14:62.
293. Isfahani AP, Arabi Shamsabadi A, Soroush M. MXenes and other two-dimensional materials for membrane gas separation: progress, challenges, and potential of MXene-based membranes. Ind Eng Chem Res. 2023;62:2309–28.
294. Al Huq MS, Gururajan B, Srinivasan P. Next-generation bioinspired 2D-MXene devices for cardiovascular disease diagnosis: a state-of-the-art review on materials interface and critical challenges. Coord Chem Rev. 2025;535:216631.
295. Zhu M, Lu C, Liu L. Progress and challenges of emerging MXene based materials for thermoelectric applications. iScience. 2023. https://doi.org/10.1016/j.isci.2023.106718.
296. Habib ML, Munshi MH, Kamruzzaman Md, Baul T, Hasan MM. Synthesis and characterization of polyvinyl alcohol-based bioplastic film incorporated with keratin extracted from duck feathers. Results Mater. 2025;27:100735.
297. Li L, Shen G. MXene based flexible photodetectors: progress, challenges, and opportunities. Mater Horiz. 2023;10:5457–73.
298. Mathew S, et al. Synthesis, mechanisms, challenges, and future prospects of Ti3C2 MXene and its heterojunctions for photocatalytic dye degradation efficiency: a comprehensive review. Materials Today Sustainability. 2023;24:100568.
299. Algaradah MM. MXene-based adsorbent materials for pollutants removal from water: current challenges and future prospects. Inorg Chem Commun. 2024;161:112113.

Publisher's note